On the impacts of ice cover on flow profiles in a bend

Berkay Koyuncu[1]

Trung Bao Le [1,2]

[1]Environmental and Conservation Sciences

College of Engineering, North Dakota State University, ND, United States

[2]Department of Civil, Construction and Environmental Engineering,

North Dakota State University, ND, United States

Key Points:

- We propose a procedure based on the quartic profile to determine shear velocity for ice-covered flows
- Under open-surface condition, our data supports for the existence of the logarithmic layer near the river bed. Under ice-covered condition, it is challenging to identify the existence of the logarithmic layers.
- The ice cover alters the secondary flow pattern, and relocates the position of the main circulation.
- Under ice-covered condition, shear stresses are elevated near banks even at relatively low discharge.

Corresponding author: Trung Bao Le - ORCID: 0000-0002-4692-5469, trung.le@ndsu.edu

Abstract

We investigate the impact of ice coverage on flow and bed shear stress profiles in a river bend. We perform field measurements using Acoustic Doppler Current Profiler (ADCP) in a bend of the Red River, North Dakota, the United States. Field campaigns were carried out under both open surface and ice-covered conditions in 2020 and 2021. Our results show that the time-averaged velocity profile follows closely the quartic solution (Guo et al., 2017) under full ice coverage. While the flow profile under open-surface condition follows closely the logarithmic law near the bed, it is challenging to identify the logarithmic layers in our measured data under ice-covered condition. Our results also show that the impact of ice coverage is most significant near both banks where the vertical velocity profile is modified significantly due to the interaction of turbulent flows with the ice cover. Our results suggest that the bend curvature and ice coverage both have significant impacts on the velocity profile as well as the distribution of the bed shear stresses. Our findings provide new insights on sediment transport processes of ice-covered rivers, especially during the break-up period when the surface coverage changes rapidly.

Plain Language Summary

As climate change continues, shorter winter is expected to result in a less number of ice-covered days for natural streams. While ice cover has been linked to a variety of eco-hydraulic issues, it is unclear on the relationship between ice coverage and changes in river hydrodynamics. Thus the understanding of ice-covered flows has become a critical issue to predict morphological and ecological conditions of river flows in cold regions. This study aims to identify the impact of ice by conducting field-scale observations and comparing with analytical models. Our results show that the ice layer alters flow patterns beneath it, which leads to active areas near banks. This new finding suggests that ice cover might play a significant role in sediment transport near banks in Spring when its extension can change sharply in a short amount of time.

1 INTRODUCTION

Ice coverage has been recognized as an important hydraulic aspect of alluvial channels for a long time (Guo et al., 2017). The role of river ice in ecological (Prowse, 2001b) , morphological (Ettema, 2002), and hydraulic aspects (Prowse, 2001a) have been well recognized. Recent evidence suggests that it plays an important role in regulating large-scale turbulent structures (Biron et al., 2019) and ultimately channel lateral migration (Turcotte et al., 2011). Under the impact of climate change, the loss of river ice (Yang et al., 2020) is expected to lead to detrimental consequences for aquatic environments (Thellman et al., 2021). Despite its importance, our understanding of icy flows is rather limited because of challenges related to field measurements. The goal of this study is to examine the impacts of ice coverage on flow profiles in a meandering bend, a common feature of the riverine system.

Field measurement of turbulent flows in rivers is challenging even under open-surface condition (Petrie et al., 2013), especially when secondary flow is observed (Moradi et al., 2019). The measurement under ice coverage poses a different set of safety and accuracy issues when instruments are placed beneath the ice layer (Biron et al., 2019). Under a fully frozen surface, it is necessary to drill holes across the ice layer in order to make the sensor submerged. In particular, it is challenging to obtain reliable data close to the ice layer as well as the river bed (Attar & Li, 2013).

As the top surface is frozen during winter (Ettema, 2002), it provides an additional layer of roughness in addition to the river bed. The presence of the ice coverage alters the spatial distribution of the entire velocity profile. Ice coverage creates a significant difference between the physical characteristics of surface and bed, forming an asymmetrical flow configuration (Chen et al., 2018; Parthasarathy & Muste, 1994). The asymmetrical flow configuration has been well studied under laboratory conditions (Hanjalić & Launder, 1972) in which the aspect ratio (width/depth) has been shown to control the overall flow dynamics.

There has been no universal law for asymmetrical flow configuration in rivers. In contrast to the logarithmic law of the open-surface case, it is unclear on the form of the time-averaged velocity profile in the asymmetrical configuration (Guo et al., 2017). There exists a maximum velocity, which typically does not locate on the symmetry plane (Tsai & Ettema, 1994; Tatinclaux & Gogus, 1983; Urroz & Ettema, 1994b). As the shape of the velocity profile is changed under ice-covered condition, its gradient near the river bed is different from the open-surface counterpart (Guo et al., 2017). Therefore, the hydraulics of ice-covered flows differs significantly (Ettema, 2002; Prowse, 2001a) from the open-surface condition.

The main structure of the velocity profile can be described in Figure 1. We denote z as the distance from a measured point to the river bed surface as shown Figure 1A. The vertical distance corresponds to the maximum velocity u_{max} is z_{max}. Under ice-covered condition, the maximum velocity location (u_{max}) separates the entire profiles into: 1) the ice layer (h_i); and 2) the bed layer (h_b) as shown in Figure 1B. Thus the total depth $H = h_i + h_b$. Note that the local depth of a measured point is $h = H - z$. The stationary boundary condition on the ice and the bed surface dictate that $u(z = 0) = u(z = H) = 0$.

Under open-surface condition, one fundamental quantity that characterizes velocity profile near the river bed (Wilcock, 1996) is the friction velocity ($u_b^\star$). It can be linked to the bed shear stress as $\tau_b = \rho(u_b^\star)^2$, which is needed to determine sediment transport processes (Chaudhry, 2007). Therefore, the evaluation of $u_b^\star$ and τ_b are frequently required in river hydraulics.

Direct measurement of the bed shear stress τ_b or shear velocity $u_b^\star$ in rivers is not feasible (Petrie & Diplas, 2016) with the current technologies. Thus many methods have been proposed (Biron et al., 1998) to calculate $u_b^\star$ indirectly from velocity measurements. Since the flow in the alluvial channel is characterized by high Reynolds numbers, turbulent statistics are typically involved in the calculation of $u_b^\star$ (A. Sukhodolov et al., 1999): (a) Turbulent Kinetic Energy (TKE) (Soulsby, 1981), (b) Reynolds stress, and (c) Wall similarity methods (López & García, 1999; Hurther & Lemmin, 2000). These methods are highly accurate and they do not assume a predetermined velocity profile. However, they require the full calculation of the Reynolds stress tensor. Therefore, precise measurement of turbulent fluctuation u' is required along the water column pointwisely. For a small or medium river (A. Sukhodolov et al., 1999), it is a tedious task to perform this type of measurement along a cross-section in a reasonable amount of time because the sensor needs to traverse systematically point-to-point. For a large river, it is not feasible to carry out such a field campaign due to the potential change of the hydrological conditions (water level and discharge), which might alter completely the turbulent regime. Thus these methods are not widely used under field conditions.

The most common method to determine $u_b^\star$ in practice is to utilize the time-averaged velocity profile to determine $u_b^\star$ via the assumption of a logarithmic layer close to the river bed (Biron et al., 1998; Petrie et al., 2013; Petrie & Diplas, 2016). The main assumption is that there exists an equilibrium layer near the river bed at which the turbulence production and dissipation balances out to give rise to the logarithmic law. In zero pressure gradient, the universal law of the wall has been verified in many laboratories and numerical simulations (Volino & Schultz, 2018). This logarithmic method does not require the acquisition of highly resolved turbulent statistics (Biron et al., 1998) and thus this procedure can be applied for many types of measurement devices including the popular Acoustic Doppler Current Profiler (ADCP) (Petrie & Diplas, 2016). Since ADCP can provide the entire velocity profile in the water column in one measurement, the sensor is kept afloat at a stationary location (fixed-vessel method) (Petrie & Diplas, 2016) for a period, which can vary from 1 to 25 minutes (Petrie et al., 2013). The time-averaged velocity profile is then fitted with the logarithmic law to find $u_b^\star$.

In order to compute shear velocities for ice-covered flows (A. Sukhodolov et al., 1999), it has been hypothesized (two-layer hypothesis) that there exist three regions: (a) two logarithmic layers near the river bed and the ice surface; and (b) the mixing (core) region at the mid-depth as shown in Figure 1B. Here, two logarithmic layers are assumed to locate near the top (ice) and bottom (river bed) surfaces. Using the two-layer hypothesis, the logarithmic law method is typically applied (Ghareh Aghaji Zare et al., 2016) separately within the ice layer (δ_i) and the bed layer (δ_b) as shown in Figure 1B. To resolve the logarithmic layers, it is required that measured data must be carried out at locations near the ice layer and the river bed (A. Sukhodolov et al., 1999). However, the validity of the two-layer hypothesis has been questioned (Urroz & Ettema, 1994a) in meandering rivers since the secondary flows (Demers et al., 2011) might alter the local velocity profiles. In addition, it has been pointed out (Guo et al., 2017) that the double log-law profile is not physical as it is not possible to satisfy the continuity condition at the maximum velocity location u_{max}. This challenge motivates the use of the entire velocity profile (Attar & Li, 2012) to derive $u_i^\star$ and $u_b^\star$ in ice-covered flows. This practice alleviates the requirement of resolving the logarithmic layer but it needs an assumption on the form of velocity distribution, which is generally not known under the field condition. To provide a physical argument for assuming the velocity profile, (Guo et al., 2017) have derived an analytical form of velocity distribution along the water column using an assumption on the distribution of eddy viscosity. However, the accuracy and reliability of this method in estimating $u_i^\star$ and $u_b^\star$ (Guo et al., 2017; F. Wang et al., 2020) has not been examined in river bends.

As the logarithmic layer is considered valid within a thickness of (δ_b) in the bed layer as elaborated in Figure 1B, it is common to use wall units to non-dimensionalize hydraulic quantities. In this approach, $u_b^\star$ and ν are used to form the velocity and viscous length scales. The friction Reynolds number based on shear velocity ($u_b^\star$), the logarithmic layer thickness δ_b, the vertical distance from the river bed z, and the non-dimensional velocity profile $u^+(z^+)$ are expressed in terms of wall units as:

$$\begin{aligned} Re_\tau^b &= \frac{Hu_b^\star}{\nu} \\ \delta_b^+ &= \frac{\delta u_b^\star}{\nu} \\ z^+ &= \frac{zu_b^\star}{\nu} \\ u^+(z^+) &= \frac{u(z)}{u_b^\star} \end{aligned} \tag{1}$$

Under laboratory condition, the logarithmic layer δ_b^+ can extend (Guo et al., 2017) up to $z^+ = 10^4$.

A similar procedure can be carried out to define the shear velocity for the ice layer as seen in Figure 1B with the shear velocity ($u_i^\star$):

$$\begin{aligned} Re_\tau^i &= \frac{Hu_i^\star}{\nu} \\ \delta_i^+ &= \frac{\delta_i u_i^\star}{\nu} \\ h^+ &= \frac{hu_i^\star}{\nu} \\ u^+(h^+) &= \frac{u(h)}{u_i^\star} \end{aligned} \tag{2}$$

Under open-surface condition, the existence of the logarithmic layer has been assumed to follow the theoretical estimate (Gao et al., 2020) as:

$$2.6Re_\tau^{1/2} \leq z^+ \leq 0.15Re_\tau \tag{3}$$

The upper bound (thickness) for the logarithmic layer is thus: $\delta_{theory}^+ = 0.15Re_\tau$.

To date, there has been no report on the thickness of the logarithmic layer under ice-covered condition.

As mentioned above, one important factor affecting the distribution of $u_b^\star$ is the effect of secondary flows (Petrie & Diplas, 2016). Laboratory experiments (Anwar, 1986) have shown that the vertical velocity profile deviates from the logarithmic law in the bend region. In complex three-dimensional flows, it is even not possible to derive $u_b^\star$ using the logarithmic hypothesis (Biron et al., 2004). The distribution of the bed shear stress (τ_b) and thus the shear velocity ($u_b^\star$) has been shown to be dependent on the local secondary flows (Stoesser et al., 2010; Bathurst et al., 1979). Since the understanding of secondary flows under ice-covered condition is limited, it is unclear how ice cover impacts the velocity and shear velocity distribution in meandering rivers.

In this work, the impacts of ice cover on flow profiles are investigated in a river bend. The main objective of this research is to uncover the impacts of ice coverage on flow profiles and secondary flow structures. Fieldworks are carried out under both open-surface and ice-covered conditions to provide the vertical velocity profiles. Whenever appropriate, the logarithmic law is invoked to derive $u_b^\star$ and $u_i^\star$. On the other hand, the applicability of the quartic solution (Guo et al., 2017) will be examined using our measured dataset. The results from these methods are compared to evaluate their compatibility in providing accurate value of shear velocities. The three-dimensional structures of secondary flows under ice coverage are also discussed to identify locations where the analytical solutions can be applied.

2 METHODOLOGY

2.1 Study area

A $2-km$ long section of the Red River near Lindenwood Park in Fargo, North Dakota was decided as the study field (Figure 2A). A pedestrian bridge locates in the middle of the apex served as the reference location (Figure 2A and 2B). At the end of the reach, there exists a United States Geological Survey (USGS) station (USGS FARGO 09020104) at the gage elevation of $262.68m$ above the North American Vertical Datum (NAVD88).

2.2 Measurement methodologies

Following the suggestion of (A. Sukhodolov et al., 1999; A. N. Sukhodolov, 2012), the fixed-vessel (FV) method (Petrie et al., 2013) was used for this study. The Acoustic Doppler Current Profiler (ADCP), Sontek $M9$, was used to measure the velocity components and bathymetry under the pulse coherent mode of 1MHz. The M9 had the following specifications: a) depth range 0.2m - 80m; b) depth accuracy 1%; c) velocity accuracy 0.002 m/s; d) cell size (0.02m -4m). In our measurement, the blank distance was set to be 0.25 m. The measured bin was adjusted automatically and varied from $0.02-0.06m$ depending on the total depth H ($H_{max} \approx 4.1m$). The signal-to-noise ratio (SNR) of all measurements were monitored online during the campaigns and also examined after the acquisition to check their reliability to avoid beam separation. The presence of signal interference near the river bed ($z \leq$ 30 cm) was significant, thus the SNR was monitored closely in this region. If the SNRs from four different sensors were different from each other by $20dB$, the data points were omitted from the calculations.

Under open-surface condition, only one cross-section was chosen at the bridge location (see Figure 2A) (O) since it was a well-defined cross-section (red line). Measurements under open-surface condition were carried out on five measurement campaigns: (a) $Oct/02/2020$ (Oa), (b) $Oct/04/2020$ (Ob), (c) $Jun/22/2021$ (Oc), (d) $Jun/24/2021$ (Od), and (e) $Jun/30/2021$ (Oe). The $M9$ was attached to a Sontek Hydroboat as shown in Figure 2B. The fixed-vessel deployment technique was implemented by taking advantage of the pedestrian bridge. The location of the sensor ($M9$) was monitored both using the on-board GPS as well as the marked locations in the bridge section. At each vertical location, the $M9$ was kept stationary for at least 600 seconds. The value of (ℓ) indicated the distance from the outer bank along the horizontal axis X as shown in Figure 3A. The details of measurements and their associate discharges are shown in Table 1.

Under ice-covered condition, measurements were conducted by opening ice holes (Figure 2C). The number of opened ice holes varied from 6 to 8 holes depending on the cross-section. Locations of the ice holes were measured from the outer (left) bank. In order to probe the three-dimensional flow structures at this location, four separate cross-sections were chosen for measurements to elucidate the three-dimensional flow structures: Ia ($Feb/19/21$), Ib ($Feb/20/21$), Ic ($Feb/21/2021$), and Id ($Feb/21/2021$). These cross-sections were separated by a distance of $6.1m$ along the North (Y) direction. To avoid bias in the measurement, a separate cross-section Ie ($Feb/21/2021$) at the bend apex, which was $310m$ away from the bridge, was selected for an additional measurement (Figure 2A). In each measurement, the Sontek $M9$ sensor was placed $0.2m$ under the ice layer. The distance from left bank ℓ at each cross-section was noted during the field survey and represented for each cross-section as seen in the diagram of Figure 2C. The period of measurement was limited to $120s$ to avoid freezing of the equipment's surface since the air temperature went below -20^0C. This low air temperature was to ensure that the ice thickness was at least $0.25m$, which was required to be safe to perform measurements. All details of the measurements were summarized in Table 1.

2.3 Data processing and flow statistics

The raw data of the M9 in text format were processed using our in-house MATLAB code to produce $1Hz$ time series. A separate MATLAB code was used to calculate flow statistics from the time series including: (a) the depth-averaged velocity profiles; and (b) the time-averaged velocity profile for each vertical location. Following the suggestion of (Petrie & Diplas, 2016), the depth-averaged value $U(T)$ and the time-average profiles for each vertical $u(z,T)$ were computed as the function of averaging period T as:

$$U(T) = \frac{1}{H}\int_{z=0}^{z=H} u(z,T)dz \tag{4}$$

$$u(z,T) = \frac{1}{T}\int_{t=0}^{t=T} u(z,t)dt \tag{5}$$

The final values of $U(T_\infty)$ and $u(z,T_\infty)$ correspond to the time-averaged value of the entire record ($T = T_\infty$). They are denoted as the long-term depth-averaged (U_∞) and time-averaged ($u_\infty(z)$) velocities, respectively, to provide a scale to indicate the range of variability of the signals. Under the open-surface condition, the total length of the measurement period T_∞ for each vertical was $T_\infty \geq 10$ minutes whereas it was only $T_\infty \approx 2$ minutes for ice-covered cases as shown in Table 1. In total, there were 50 and 55 time series under the under open-surface and ice-covered conditions, respectively. Finally, the calculation of the shear velocity $u_b^\star$ and $u_i^\star$ was based on the values of $u_\infty(z)$ as shown in the next sections. If otherwise noted, the notation ∞ is dropped to simplify the discussion of the vertical velocity as $u(z)$.

2.4 The logarithmic law of the wall

The logarithmic law of a rough wall (Shen & Lemmin, 1997) is:

$$\frac{u(z)}{u_b^\star} = \frac{1}{\kappa}\ln\frac{z}{z_0} + \beta \tag{6}$$

where $\kappa = 0.39$ is the Von Karman constant, β is the additive constant ($\beta = 8.5$). The parameter z_0 is the roughness length. In natural rivers, this logarithmic law is typically considered valid within a distance δ_b from the river bed. Typically, δ_b varies from 20%

to 50% (Petrie & Diplas, 2016; Petrie et al., 2013) of the total depth H. Under field conditions, the value of δ_b is not known in advance. Therefore, a procedure to determine δ_b will be discussed below.

The shear velocity ($u_b^\star$) and the roughness length (z_0) are found by fitting the Equation 6 with the measured data ($u(z)$) in each vertical. A common procedure (Petrie & Diplas, 2016) is to use the linear regression line between the measured value of $u(z)$ and $ln(z)$. As the linear regression line is known, the values of $u_b^\star$ and z_0 are computed as:

$$u_b^\star = \kappa m \tag{7}$$

$$z_0 = exp[8.5\kappa - \frac{\gamma}{m}] \tag{8}$$

Here, γ and m are the intercept point and the slope of the best-fit regression line, respectively.

Under open-surface condition, the agreement between the linear regression line and the measured data must satisfy (Petrie & Diplas, 2016) the following criteria: (1) the correlation coefficient $R^2 > 0.9$, (2) a positive shear velocity $u_b^\star > 0$, and (3) a realistic value of z_0 ($0.001m < z_0 < 10m$). In brief, the detailed steps of the logarithmic method for both open surface and ice-covered conditions are as follows:

- *Step 1*: Assume a value of δ_b ranging from $0.05H$ to $1.0H$ with an increment of $0.05H$ for each trial. The fitting to the logarithmic law is performed only when there is sufficient data in the logarithmic layer δ_b. The presence of at least five points within δ_b is required.
- *Step 2*: The velocity magnitude $u(z)$ is plotted against the $\ln(z)$ at every measurement point. Available MATLAB functions, *"polyfit"* and *"polyval"* are called to perform linear regression from the selected points in Step 1, to obtain the linear fitting parameters m and γ.
- *Step 3*: The shear velocity is computed as $u_b^\star = \kappa m$.
- *Step 4*: Equation 8 is used to compute the roughness length (z_0) using the values of the parameters γ and m.
- *Step 5*: R^2 value is computed from the linear fitting of Equation 6 in comparison to the corresponding measured data. The values of R^2, $u_b^\star$, and z_0 are checked si-

multaneously to validate the presence of the logarithmic layer. The following values are validated with $R^2 > 0.9$, $u_b^\star > 0$, and $0.001m < z_0 < 10m$.

- *Step 6*: Record the value of R^2 and δ_b. If R^2 is greater than 0.9 then go back to Step 1 with an increment in the value of δ_b. If not, go to Step 7.
- *Step 7*: Find the value of δ_b that gives the highest R^2. Compute $u_b^\star$ and its associated z_0.

2.5 Quartic profile for asymmetrical flows

The quartic profile of (Guo et al., 2017) is formulated using the relative distance η, which is defined as $\eta = 2\frac{z}{H}$. The maximum velocity location is defined in term of its relative distance as: $\eta_{max} = \frac{2z_{max}}{H}$.

A non-dimensional parameter (λ) is used to represent the asymmetry of the flow profile as:

$$\lambda = \sqrt{\frac{2}{\eta_{max}} - 1} \tag{9}$$

Here $\lambda = \frac{u_i^\star}{u_b^\star}$ quantifies the asymmetry of shear stress on the top ($u_i^\star$) and bottom ($u_b^\star$) surfaces. Therefore, the value of λ is important in determining the shape of the velocity profile. An interim parameter ($\alpha = \frac{1-\lambda}{\lambda-\lambda^{2n}}$) is also used to reflect this asymmetry. In this equation, n is the mixing turbulent intensity. While n can vary depending on the turbulent flow condition, it is found for the symmetric flow condition as $n = 5/6$ (Guo et al., 2017).

The location of the zero shear stress plane (η_c) typically does not coincide (Hanjalić & Launder, 1972) with the maximum velocity location. However, it is (Guo, 2017) assumed that the location of the maximum velocity and the zero shear stress plan is identical. Thus, this location can relate to λ as $\eta_c = \eta_{max} = \frac{2}{(1+\lambda^n)}$ with $u_c = u_{max}$.

The quartic solution find the best fit velocity profile (u_f) to the measure data. u_f can be written in terms of its non-dimensional form u^+ with the help of the bed shear velocity $u_b^\star$ as:

$$\frac{u_f(\eta)}{u_b^\star} = u^+(\eta) \tag{10}$$

Therefore, the bed shear velocity is used to provide a non-dimensional profile $u^+ = u/u_b^\star$. For example, the critical velocity at the critical depth η_c is non-dimensionalized as ($u_c^+ = u_c/u_b^\star$).

The main contribution of (Guo et al., 2017) is that the dimensionless velocity profile (u^+) is suggested to follow the analytical solution:

$$u^+(\eta) = u_c^+ + \phi(\eta) \tag{11}$$

Here the velocity profile function ($\phi(\eta)$) is derived for infinitely long and straight channel as:

$$\phi(\eta, \lambda) = \frac{1}{\kappa}\{\ln(\frac{\eta}{\eta_c}) + \lambda \ln \frac{2-\eta}{2-\eta_c} - \frac{1+\lambda}{2}\ln[1+\alpha(1-\frac{\eta}{\eta_c})^2] - (1-\lambda^{n+1})\sqrt{\alpha}\tan^{-1}\sqrt{\alpha}(1-\frac{\eta}{\eta_c})\} \tag{12}$$

The shear velocity at the river bed can be calculated as:

$$u_b^\star = \frac{\sum_i \phi(\eta_i, \lambda)(u_i - u_c)}{\sum_i \phi^2(\eta_i, \lambda)} \tag{13}$$

Our detailed steps for fitting the vertical velocity profile under the ice-covered condition with the ADCP data are as follows:

- Step 1: In each vertical location, the entire measurement points are selected from the value of $u(z)$ as discussed in Section 2.3. The number of available points along the depth is dictated by the measured cell size ($0.02-0.06m$), which is automatically adjusted by the M9 sensor. Note that in each cross-section Ia, Ib, and Ie, there are two separate measurements $M1$ and $M2$ (2 minutes each) at every vertical locations (see also Table 1). In such cases, the fitting procedure is performed on the averaged value of $M1$ and $M2$. Since the number of points along the depth can be slightly different between the first measurement $M1$ and the second measurement $M2$, we need to reconstruct the averaged profile of $M1$ and $M2$. First, the distance z is converted into the relative distance ($0 \leq \eta \leq 2$). The value of the entire depth is then divided into an uniform intervals $N = 100$ in each vertical location as η_i ($i = 1 \rightarrow N$). For each measurement $M1$ or $M2$, a procedure is carried out to map the measured data $u(z_i)$ into the interpolated value $u(\eta_i)$ at the location η_i using the MATLAB function, "*interp1*" with piecewise cubic spline interpolation. Second, the averaged value of $\bar{u}(\eta_i)$ between the measurement $M1$ and $M2$ is finalized for further processing.

- *Step 2:* To further smooth out the variation of $\bar{u}(\eta_i)$ long the depth, a Fourier filtering method is performed on $\bar{u}(\eta_i)$ with the first 5 frequencies to obtain the filtered value $\widetilde{u(\eta_i)}$.
- *Step 3*: The location of the maximum velocity $\widetilde{u_{max}}$ in the vertical axis (η_{max}) is identified in this step. Since the value of η_{max} controls the fitting accuracy, it is important to investigate the sensitivity of the fitting procedure with η_{max} systematically. The value of η_{max} is varied within the 10% range.
- *Step 4*: The parameters λ and α are computed according to Equation 9 with the chosen value of η_{max}.
- *Step 5*: The location of the critical position of the eddy viscosity (η_c) is assumed to be the same as the value of η_{max}. Accordingly, the critical velocity is set to be equal to the maximum velocity ($u_c = \widetilde{u_{max}}$).
- *Step 6*: The velocity distribution function ($\phi(\eta_i)$) is computed by Equation 12.
- *Step 7*: The shear velocity at the river bed $u_b^\star$ is computed by Equation 13 using the values of $\widetilde{u}_i$ and u_c. The non-dimensional critical velocity is computed as $u_c^+ = \frac{u_c}{u_b^\star}$.
- *Step 8*: The non-dimensional velocity profile ($u^+(\eta_i)$) is produced by Equation 11.
- *Step 9*: The fitted velocity magnitude ($u_f(\eta_i)$) at the depth η_i is computed by Equation 10.
- *Step 10*: The correlation coefficient factor R^2 between the measured ($u(z)$) and fitted ($u_f(z)$) velocity profiles is computed. Record the dependence of the value R^2 on η_{max}.
- *Step 11*: Go back to Step 3. The iterative process will terminate until the highest correlation value R^2 is obtained with the selected η_{max}.

2.6 Estimation of $u_b^\star$ from depth-averaged velocity (friction method)

The computation of boundary shear stress is a challenge since the ADCP is not able to measure accurately the flow velocities near the river bed due to the side-lobe interference. This challenge leads to the use depth-averaged velocity vector $\vec{U}(U_x, U_y)$ (Engel & Rhoads, 2016) to estimate $u_b^\star$ under open-surface condition. The procedure is as follows:

$$
\begin{aligned}
C_f &= [\alpha_r (\frac{H}{z_0})^{\frac{1}{6}}]^{-2} \\
\tau_{bx} &= \rho C_f U_x \sqrt{U_x^2 + U_y^2} \\
\tau_{by} &= \rho C_f U_y \sqrt{U_x^2 + U_y^2} \\
\tau_b &= \sqrt{\tau_{bx}^2 + \tau_{by}^2} \\
u_b^\star &= \sqrt{\frac{\tau_b}{\rho}}
\end{aligned}
\tag{14}
$$

where, ρ, C_f, and z_0 are the fluid density, the friction coefficient, and the roughness height, respectively. The coefficient α_r is set equal to 8.1 (Parker, 1991). The equivalent roughness height z_0 is estimated as $2.95 \times d_{84}$ (Whiting & Dietrich, 1990). The value of d_{84} is computed from the USGS field survey data as $d_{84} \approx 2.088mm$ (Galloway & Nustad, 2012; Blanchard et al., 2011). U_x and U_y are the two components of the depth-averaged velocity vector ($\vec{U}$) along the X and Y, respectively. The corresponding components of the magnitude shear stress (τ_b) are defined as (τ_{bx}) (cross-stream) and τ_{by} (streamwise). Since the depth-averaged velocity $\vec{U}$ is available for all vertical locations, this friction method can be applied anywhere. The Equation 14 indicates a direct correlation between $u_b^\star$ and U (Chauvet et al., 2014).

3 RESULT

As the measured cross-sections locate in a meandering bend, the impact of the channel curvature is significant. This effect is presented using the depth-averaged velocities U under open-surface condition as shown in Figure 3. Overall, the depth-averaged profiles are asymmetrical toward the outer bank. At high discharges (Oa and Ob), the maximum velocity is visible in the left part of the thalweg. Note that $Q_{Oa} \approx Q_{Ob}$ and thus the velocity profiles of Oa and Ob are closely similar. At low flow conditions (Oc, Od, and Oe), such an asymmetry is not distinct as the flow in the thalweg is nearly uniform. In the following sections, the characteristics of the vertical profiles will be examined at each location in the cross-sections. First, the statistical analysis is carried out to determine if the measured data is sufficient to generate reliable values for U and $u(z)$. Second, the validity of the logarithmic law is examined under open-surface condition. Third, the presence of the double log-law is investigated for the ice-covered cases. Fourth, we revisit the quartic solution and its applicability to derive shear velocity for ice-covered condition in the current study. Finally, we address the changes in secondary flow patterns under the impacts of the ice cover.

3.1 Data statistics

Under open-surface condition, the results show that the value of the time-averaged velocity $u(h, T)$ at all locations h along the depth does depend on the averaging period T. Figure 4 illustrates that the $u(h, T)$ oscillates near the free surface ($h = 0.26m$) and the bed ($h = 3.44m$) at the stations of Oa_5 and Ob_5 when $T < 200$ seconds. This oscillation, however, remains in the $10\% u_\infty(h)$ range. In particular, $u(h, T)$ converges to its long-term values $u_\infty(h)$ within $\pm 5\%$ in the first 100 seconds. The value at the mid-depth $u(h = 1.82m, T)$ converges even more quickly to the long-term value. In contrast to the time-average velocity, the depth-averaged $U(T)$ converges rapidly to its long-term value U_∞ without any significant oscillation within the first minute. As shown in Figure 3, the obtained depth-averaged profiles of Oa and Ob are consistent given closely similar flow discharges. A similar observation is applied for Oc and Od. In brief, the period $T \approx 200$ seconds is sufficient for the time-averaged profile $u(h, T)$ and depth-averaged $U(T)$ to attain their accuracy within $\pm 5\%$ of their long-term values.

The variation of the vertical velocity profile $u(h, T)$ under different periods of averaging T is shown in Figure 5. To examine the convergence of the vertical profiles as a function of the period T, four different periods are selected: $D - 1$ ($t = 0 \rightarrow 120$ seconds) ; $D - 2$ ($t = 200 \rightarrow 320$ seconds); $D - 3$ ($t = 0 \rightarrow 400$ seconds); and $D - 4$ ($t = 0 \rightarrow 620$ seconds) for the verticals Oa_5 (Figure 5A) and Oc_6 (Figure 5B). In both Oa_5 and Oc_6, there exists a significant complex flow profile near the free surface ($h < 1.5m$). In this region, the shape of the vertical does dependent significantly with the averaging period T. Comparing the period $D - 1$ and $D - 2$, which last 120 seconds, the time-averaged profiles ($u(h, T)$) are significantly different, especially in the near surface region. In the near bed region ($h > 2m$), the shape of the profile is less sensitive to the choice of the period T. Indeed, the profile ($u(h, T)$) becomes nearly identical between $D-3$ and $D-4$ when the value of T is extended to 620 seconds. In other vertical locations, the convergence of velocity profiles is similar to ones as seen in Figure 5. Therefore, a period of 600 seconds (10 minutes) is sufficient to obtain the velocity profile convergence under open-surface condition.

Under the ice-covered condition in Figure 6, the total length of the measurement period T_∞ is limited to approximately 120 seconds. Therefore, there exists a larger variation of $U(T)$ and $u(h,T)$ from their respective long-term values. As seen in Figure 6, two independent measurements ($M1$ and $M2$) of the same ice hole Ib_7 at the depth $h = 1.64m$ are shown. It can be seen that the ratios $\frac{U(T)}{U_\infty} \geq 10\%$ and $\frac{u(h,T)}{u_\infty(h)} \geq 20\%$ for both $Ib_7 - M1$ and $Ib_7 - M2$ at the early stage from $T = 0$ to $T = 100s$. Here, it is seen that the stabilization of $u(h,t)$ and $U(T)$ can only attain when $T > 100$ seconds. For other ice holes, their running statistics also show a similar behavior. There exist a significant variation of $\frac{U(T)}{U_\infty}$ and $\frac{u(h,T)}{u_\infty(h)}$ within $\pm 10\%$ in the first minute. The values of $U(T)$ and $u(h,T)$ converge in a synchronous fashion only when $T > 100s$. In brief, it is evident that the duration of measurement $T = 120$ seconds has a significant impact on the velocity profiles.

3.2 The universality of the logarithmic law under open-surface condition

Under the open-surface condition, the logarithmic fitting is summarized in Table 2. The presence of the logarithmic law is validated in most measurements of Oa, Ob, Oc, Od, and Oe with high degree of agreement ($R^2 \geq 90\%$) in the thalweg. It can be observed in Table 2 that the logarithmic law is observed in all sufficiently deep locations ($H \geq 3.5m$). In these locations, the logarithmic layer (δ_b) remains in 20% of the total depth ($\delta_b \approx 20\% H$). In the majority of the stations, the logarithmic layer can extend up to approximately 50% of the total depth. Therefore, the law of the wall is considered applicable for most locations in the bend thalweg regardless of the flow discharge.

To further examine the universality of the logarithmic law, the extension of the logarithmic layer is presented in Figure 7 in terms of wall units. Three vertical locations are shown in different measurement dates as Oc_4, Od_7, and Oe_5. The measured data fit excellently well with the logarithmic law as evidenced by the correlation between the $u^+(z^+)$ and z^+ for these cases in the range of $4000 \leq z^+ \leq 10,000$. However, the separation from the logarithmic law initiates at different values of z^+ depending on the profile. For example, the separation starts at $z^+ \approx 15,000$ for the case Oc_4 and Oe_5. However, it starts much later at $z^+ \approx 20,000$ for the case Od_7. Here the value of the shear velocity $u_b^\star$ is found to vary around $0.01m/s$. Consequently, the local value of Re_τ^b (Equation

1) varies from $8,000$ to $60,000$. As shown in the Table 2, the logarithmic layer (δ_b^+) obeys the theoretical limit (Equation 3) excellently well with $\delta_b^+ \geq \delta_{theory}^+$ for all cases.

There are vertical locations that do not follow the logarithmic law (Oa_6, Oa_7, Oa_8, Oa_9, Ob_4, Oc_3). In these profiles, it is not possible to perform the logarithmic fitting with the listed constraints in section 2.4. They are mostly located near the inner and outer banks where the secondary flows are strong. The deviation of the velocity profiles of these locations from the logarithmic law will be discussed in section 3.5.

3.3 The double log-law under ice-covered condition

In contrast to the open-surface condition, the presence of the logarithmic layer is found using the criteria in section 2.4 only in limited locations near the bed as shown in Table 3. In those locations, the logarithmic layer δ_b extends well beyond 20% and up to 50% of H. Interestingly, the value of $u_b^\star$ is found to be significantly larger near banks $u_b^\star \approx 0.04m/s$ (Ib_7 and Id_8) than ones in the thalweg region (Ia_6, Ib_2, Ib_6, Ic_2, Id_6) in which $u_b^\star$ varies around 0.01m/s. In brief, our data confirm the presence of the logarithmic layer near the river bed in a limited number of ice holes.

The logarithmic layer near the ice cover is found in a larger number of vertical stations as shown in Table 4 in all cross-sections Ia, Ib, Ic, Id and Ie. In these locations, the logarithmic layer extends mostly up to 20% of the total depth H in general. However, the value of the shear velocity $u_i^\star$ is generally lower than $0.01m/s$. In short, the applicability of the logarithmic law for the ice layer is different from the river bed layer.

The logarithmic profiles under ice-covered condition are shown in Figure 8. Far from the wall, their deviation from the logarithmic profile is indicated by a plateau (the central core region). Near the ice cover (top inset) in Figure 8A, the logarithmic layer in Ic_5 and Id_5 terminates at the depth $h^+ \approx 4000$. Beyond $h^+ > 4000$, the velocity profile reaches a short plateau that remains in the range of $4000 \leq h^+ \leq 10,000$. In the bed layer in Figure 8B, a similar behavior of the velocity profile is observed where the logarithmic layer terminates around $z^+ \approx 15,000$ (Ib_6 and Id_6). The plateau section of Ib_6 extends toward $z^+ \approx 30,000$ whereas it is limited to $20,000$ for Id_6. The thickness of the logarithmic layers in wall units (δ_i^+ and δ_b^+) for applicable ice holes are summarized in Table 3 and Table 4 for the bed and the ice layer, respectively. Here, the theoretical bounds (Equation 3) are well below the measured values of δ_i^+ and δ_b^+. Thus the Equation 3 is effective in predicting the potential thickness of the logarithmic layer under ice coverage.

3.4 The applicability of quartic profiles for ice-covered flows

Overall, the entire profiles in almost all ice holes follow closely the quartic solution as shown in Figure 9 and Table 5 following the fitting procedure as discussed in section 2.5. Surprisingly, the quartic solution works well even in the shallow parts of banks (Id_2 and Id_7 in Figure 9, for example). In certain locations (Ia_5 and Id_2), the existence of the maximum velocity u_{max} is evident. However, it is not straightforward to assign a unique value of u_{max} in the time-averaged velocity profile for other cases. Here, the optimization of R^2 (see section 2.5) is useful in justifying the value of η_{max}. As shown in Table 5, the u_{max} location does not typically coincides to the symmetry plane ($\eta = 1$). Rather, the value of η_{max} is frequently greater than 1 and indicates that the maximum velocity appears closer to the ice layer. The asymmetry of the velocity profile is also evident as the value of $\lambda = \frac{u_i^\star}{u_b^\star}$ is mostly less than 1 as shown in Table 5. Therefore, our data supports for a general use of the quartic form for ice-covered flow profiles in rivers.

3.5 The structures of secondary flow

In the vicinity of the bridge, the cross-sections are designed to align to the X direction so that the three-dimensional flow structures can be visualized by the velocity vectors in the (X, Z) planes. Here, time-averaged East (u_x) and Up (u_z) velocity components are used to visualize the secondary flow structure.

Under open-surface condition, our results show the signature of a classical circulation in the bridge cross-section under high discharge (Oa and Ob) as shown in Figure 10A (upper panel). On Oa, the secondary flow contains a large vortex occupying the entire thalweg area from the river bed to the free surface. In Ob, the secondary vortex is limited closer to the bed. This circulation rotates in the counter-clockwise direction. In Oa, the signature of this circulation locates near the vertical Oa_6 to Oa_9. In Ob, the circulation locates at the vertical Ob_4 to Ob_6. In other words, the location of the main circulation is sensitive to the change in flow discharge. The main circulation moves toward the center of the thalweg as the discharge decreases (Oc, Od, and Oe - see Table 1) as shown in Figure 10B (lower panel). In brief, the migration of the main circulation is significant as the water level changes.

In addition to the main circulation, our data indicates a strong convergent flow from the outer and inner bank toward the thalweg in Figure 10. In all measurements (Oa, Ob, Oc, Od, and Oe), there exists a strong lateral flow from the outer and inner bank toward the thalweg. The magnitude of this later flow component (u_x) is significantly large (up to $0.2 m/s$) near the outer bank (Oa). It does reduce to a value of $0.14 m/s$ at lower discharges (Oc, Od, Oe). The lateral flow from the inner bank toward the thalweg can be found at a much lower velocity magnitude ($0.04 m/s$) in Oa, Ob, Oc, Od, and Oe. In brief, the flow convergent pattern is also a persistent characteristic of the cross-section.

Our data indicates a significant impact of the ice cover on the secondary flow pattern. Since the cross-section Ia, Ib, Ic, and Id are parallel and separated from each other, it is possible to infer the three-dimensional flow structure at the study site as shown in Figure 11. Under ice coverage, both the main circulation and the flow convergence pattern are altered. Weak circulations are found in Ib (between Ib_1 and Ib_2) and Id (between Id_2 and Id_3). These circulations, however, rotate in the opposite directions. The flow convergence pattern is observed in Ia but it does not appear in other cross-sections. The signature of the circulation completely vanishes in Ic, which shows only a strong flow convergence from the inner bank toward the outer bank. Therefore, the secondary flow pattern varies drastically from one cross-section to another in the ice-covered bend.

3.6 Shear velocity distribution in the bend

Under open-surface condition, the bed shear velocity ($u_b^\star$) is derived using the logarithmic method as summarized in the Table 2. At high discharge (Oa and Ob), $u_b^\star$ can be as high as $0.04 m/s$. Despite a slight difference in the value of Q_{Oa} and Q_{Ob}, the distribution of $u_b^\star$ across the cross-section is consistent. In both measurements (Oa and Ob), there exists a strong skewed distribution of the shear velocity toward the outer bank as shown the trend line in Figure 12A. The location of the maximum $u_b^\star$ (Oa_2) does not coincide with the maximum depth-averaged velocity location (Oa_4 and Ob_4) (see also Figure 3). The value of $u_b^\star$ decreases gradually from the outer bank to the thalweg toward the value of $0.01 m/s$, but it slightly increases near the inner bank. This trend is not observed under low discharges (Oc and Od) in Figure 12B, which shows that $u_b^\star$ varies in a small range from $0.005 m/s$ to $0.015 m/s$ in the thalweg. In brief, a higher discharge leads to a skew $u_b^\star$ distribution with a large magnitude increase (up to four folds) near the outer bank.

Under ice-covered condition, the value of $u_i^\star$ and $u_b^\star$ are derived from two separate methods: i) the logarithmic law (section 2.4); and ii) the quartic profile (section 2.5). The derived value of shear velocities are listed in Table 4 for all cross-sections Ia, Ib, Ic, and Id. On both the ice and the bed layers, the quartic solution can provide the value of $u_i^\star$ and $u_b^\star$ in the majority of ice holes as seen in Figure 13. On the contrary, the logarithmic method (solid diamonds) can provide only at certain locations due to the stringent constraints (see section 2.4) as seen in Table 3. For both $u_i^\star$ and $u_b^\star$, the logarithmic method yields a significantly higher value in comparison to the quartic solution as indicated in Figure 13. Both the logarithmic and the quartic methods indicate that $u_i^\star$ and $u_b^\star$ are elevated near banks. In particular, $u_b^\star$ can increase from 0.01m/s (thalweg) to approximately 0.05m/s near the inner bank. Therefore, shear velocity magnitude varies greatly across the cross-section under ice coverage.

4 DISCUSSION

Ice coverage is an essential component of river hydraulics (Ettema, 2002; Smith & Ettema, 1995; J. Wang et al., 2008). The impacts of ice on flow dynamics in rivers has recently drawn significant attention (Lauzon et al., 2019) from a wide range of viewpoint such as hydrological (Beltaos & Prowse, 2009), morphological (Chassiot et al., 2020; Kämäri et al., 2015), ecological (Knoll et al., 2019) applications. Under the impact of climate change, global coverage of river ice has declined sharply (Yang et al., 2020; Peng et al., n.d.) potentially leading to a large-scale transformation of river dynamics in cold regions, especially during spring when snow and ice thaw (Lotsari et al., 2020). Changes in river ice dynamics might lead to new morphological evolution of river deltas in cold regions (Lauzon et al., 2019) as it is known that ice coverage alters sediment transport regime (Lau & Krishnappan, 1985; Turcotte et al., 2011). However, field measurement of ice-covered flows is challenging and thus there are limited data on flow profiles to date (Ghareh Aghaji Zare et al., 2016; Lotsari et al., 2017; Biron et al., 2019). Therefore, this work is intended to revisit this important problem using a modern approach of turbulent flows.

4.1 The logarithmic layer under open-surface condition

Our data support the existence of a universal logarithmic layer (Marusic et al., 2013) for the current site. In particular, our results in Table 2 show that the logarithmic layer is applicable for vertical locations with sufficient depth ($H \geq 3.5m$) in the thalweg. In these locations, the logarithmic layer is easily detectable as it accounts for a significant portion of the depth (up to 1.5m as shown in Figure 5). As demonstrated in Figure 7, stations Oc_4, Od_7, and Oe_5 all follow closely the logarithmic profile. It has been known that the logarithmic law might be valid for the majority portions of the flow depth (Biron et al., 1998) in laboratory conditions. The value of δ_b is suggested to be 10 to 20 percent of the total depth (Biron et al., 1998, 2004) under field conditions. Our results show that the logarithmic can extend up to half of the total depth ($\delta_b/H = 50\%$) in higher flow rate (Oa and Ob - see Table 3). On the other hand, the logarithmic layer only accounts for 20 - 35% of the depth at lower flow discharge (Oc, O_d, and O_e). Therefore, the logarithmic layer can extend to a significant distance from the bed, especially in the thalweg.

A closer examination of the logarithmic layer thickness in wall units shows that it follows closely the theoretical bounds in Equation 3. Our results in Table 2 and Figure 7 show that the upper bound is applicable for the current site well. In fact, the logarithmic layer can extend well beyond the $0.15Re_\tau$ limit in many cases as shown in Table 2. Note that the value of $u_b^\star$ (and thus Re_τ) can be estimated using the Equation 14 from the depth-averaged velocity U. Therefore, our data suggests that the Equation 3 can serve as an estimation for the logarithmic layer thickness if the velocity profile $u(z)$ is not available.

It is known that complex flow fields in shallow areas or rapidly changing bathymetry (Stone & Hotchkiss, 2007; Biron et al., 1998) can lead to the deviation from the logarithmic law (Biron et al., 2004) due to the presence of secondary flows (Petrie & Diplas, 2016). In the presence of complex bathymetry with an adverse pressure gradient, the equilibrium layer could become very thin or completely vanish. Thus the logarithmic law might not exist in certain locations (Biron et al., 1998; Bagherimiyab & Lemmin, 2013). In meandering rivers, secondary flows (Petrie et al., 2013) might impact the distribution of the vertical velocity profile. The absence of the logarithmic layer is also shown to coincide with a strong presence of secondary flow circulation at our site (Oa_6, Oa_7, Oa_8 - see Figure 10A). In particular, the secondary flow is significantly strong $u_x \geq 0.1m/s$ in Oa and Ob for locations near both the outer and inner banks (see Figure 14 for station Oa_1, Oa_2, Oa_8). The impact of flow convergence from both banks on the vertical profile is demonstrated in Figure 5. While the variation of the vertical profile in the first $1.5m$ depth is minimal in Oa_5, there is a significant deviation of the profile from the logarithmic law near the surface of Oc_6 (Figure 5B), which is a common signature of secondary flows. This behavior is consistent with field observation of (Chauvet et al., 2014), which indicates that the degree of deviation depends on the distance to banks. Thus our results show that it is challenging to perform the logarithmic fitting near both banks even under open-surface condition when the flow depth is limited.

In laboratory condition (Flack & Schultz, 2010) or numerical simulation (Ma et al., 2021), the value of the equivalent roughness height, z_0, can be related to the physical roughness (Flack & Schultz, 2010). However, it has been shown (Petrie & Diplas, 2016) that the value of z_0 cannot be determined reliably using field measurement data (Petrie et al., 2013). Indeed, our fitting procedure in section 2.4 results in a large variation of z_0 over several orders of magnitude as summarized in Table 2. The obtained values of z_0 can vary from $1.0 \times 10^{-4} m$ to the order of $10.0m$. This range of obtained z_0 does not agree with the measured sediment grain size at the site, which has $d_{50} \approx 0.5mm$ (Galloway & Nustad, 2012). These results indicate that the fitting procedure cannot reproduce a reliable value for z_0. This result also justifies the use of the measured value of d_{84} in Equation 14 to estimate the shear velocity.

4.2 The challenge of using logarithmic fitting for ice-covered flows

It is striking that the theoretical bound for δ_i^+ and δ_b^+ (Equation 3) is highly effective. As shown in Table 3 and Table 4, the limit of δ_{theory}^+ is satisfied in all available cases for both the ice and river bed layers. This highlights a potential use of the Equation 3 in examining the presence of the logarithmic layers in ice-covered flows. As the value of $u_b^\star$ can be estimated from the quartic method (section 3.4), the value of δ_{theory}^+ can be deduced from the Equation 3. Therefore, the physical value of δ_{theory} can be recovered. This estimated value of δ_{theory} can guide field measurement in capturing sufficient data in the area of interest.

As the logarithmic fitting is the standard method for estimating $u_b^\star$ in straight channel in open-surface condition (Petrie & Diplas, 2016), it is not clear how to estimate $u_b^\star$ under ice coverage (A. Sukhodolov et al., 1999; Attar & Li, 2012; Ghareh Aghaji Zare et al., 2016), especially in river bends (A. N. Sukhodolov, 2012). Previous works (Ghareh Aghaji Zare et al., 2016; A. Sukhodolov et al., 1999) have assumed the double log-law and used the logarithmic fitting for ice coverage to derive $u_b^\star$. Our results in Table 3 and Table 4 indicate that only few vertical stations are qualified to perform logarithmic fitting using our data. The strict requirement of the logarithmic fitting thus does not allow the recovery of $u_b^\star$ value for ice-covered condition in all ice holes. The reason for this challenge might be the presence of the secondary flows as shown in Figure 11. Under ice-covered condition, the magnitude of the secondary flow is approximately $0.1m/s$, which is in the same order as the streamwise component. Field measurements (A. Sukhodolov et al., 1999; A. N. Sukhodolov, 2012; Demers et al., 2011) have shown that complex three-dimensional flow might arise in river bend with ice-covered condition. This complex flow field (Biron et al., 1998, 2004) might deviate the near-wall profiles from the classical logarithmic law. Therefore, it is critical to find a robust method to estimate the value of $u_b^\star$ under field condition.

4.3 The performance of quartic solution

It has been recognized (Biron et al., 1998) in early measurements that the logarithmic method requires sufficient data in the boundary layer. This requirement is typically not satisfied in field measurements (Attar & Li, 2012) as it is challenging to obtain measured data near the river bed and the ice layer. Our data in Figure 9 shows that the quartic solution agrees well with field measurement. As it uses the entire velocity profile, the quartic solution can be applied in the majority of ice holes. Note that the quartic solution is designed (Guo et al., 2017) so that it coincides to the logarithmic layer in the limit of $z^+ \to 0$. This feature relaxes the strict requirement of section 2.4. Therefore, the quartic solution can provide an estimation for the shear velocity $u_b^\star$ even if there are limited measurements along the vertical profile.

One important assumption of the quartic solution is the separation of flows in the ice and the bed layer by a distinct maximum velocity location $u_{max}(z_{max})$. As shown in Figure 1, the velocity profile is governed by different sets of shear velocities (A. Sukhodolov et al., 1999; Guo et al., 2017; Ghareh Aghaji Zare et al., 2016). The presence of u_{max}

in the analytical solution is apparent because the shear stress distribution along the depth is assumed to be linear (Guo et al., 2017). However, it is not clear whether or not a distinct u_{max} is evident in field measurements. Our results show that it is challenging to determine the location z_{max} from our field data since the time-averaged profile does not typically show a distinct u_{max}. While our fitting procedure attains good agreement ($R^2 \geq 0.9$) with measurement data, the determination of u_{max} location does affect the overall shape of the profile. The maximum velocity location η_{max} is the critical factor to attain a high value of R^2. In fact, the value of u_{max} and its position in near-bank locations are usually determined decisively as shown in Figure 9 (Id_2). However, the minimal variation of the velocity profile $u(z)$ in the mixing core region prevents a straightforward approach to locate η_{max} (Ic_4) in the thalweg. Therefore, an iterative procedure as shown in Section 3.4 is necessary to obtain the maximum value for R^2. The difficulty of locating a single value for η_{max} also highlights the limitation of the quartic method. It is required that the velocity profile has a distinct maximum value, which is not guaranteed in the presence of complex bathymetry. The strong secondary flow as illustrated in Figure 11 near Ia_5, Ic_4, and Id_7 might deviate the vertical velocity profiles from the quartic form.

4.4 Secondary flow patterns under ice coverage

Comparing our results in Figure 10 and Figure 11, it is evident that the ice cover adds further complexities in the secondary flow patterns. While the flow convergence pattern is still visible at Ia, the secondary flow patterns at other cross-sections vary greatly in a short distance of approximately 20 meters. These results indicate that the large-scale flow structure of the entire reach has been modified with the presence of the ice cover. There is no apparent existence of a large-scale circulation at Ia, Ib, and Ic as shown in Figure 11. A circulation reemerges at Id near the outer bank but it is also accompanied by a change in the flow convergence pattern. The intermittent appearance of the circulation suggests that the large-scale circulation is truly a local phenomenon, which could depend on the bathymetry and the flow depth.

Laboratory experiment (Urroz & Ettema, 1994a) suggests that the secondary flow under ice-covered condition could have a special structure (double-stacked) where two sets of vortices are found on top of each other in the thalweg. Field measurements of (Demers et al., 2011) suggest that the double-stacked vortices might exist at the bend entrance.

However, our results in Figure 11 do not support the existence of such a structure in this case in all cross-section Ia, Ib, Ic, and Id. Our result only shows a single vortex in Id close to the outer bank. It has been shown (Lotsari et al., 2017) that flow depth can alter the secondary flow pattern of ice-covered flows at river bends by changing the direction of the high-velocity core(Attar & Li, 2013). Therefore, the disagreement from our measurements with the laboratory experiment of (Urroz & Ettema, 1994a) might be explained by the difference in aspect ratio between field and laboratory scales. The aspect ratio (width/depth) of the cross-section in our case is $AR \approx 10$, which is much larger than the ones in the experiment of (Urroz & Ettema, 1994a). Thus the double-stacked vortices might appear only at certain aspect ratios of river cross-sections.

4.5 Shear stress distribution

In the literature, the period of ice coverage is assumed to be a quiescent period of sediment transport (Ettema, 2002) since the value of $u_b^\star$ is assumed to be smaller than the open-surface counterpart. Comparing the Figure 13B and Figure 12B under similar flow discharges, it is evident that the ice coverage contributes to a significant increase of $u_b^\star$ near banks. The value of $u_b^\star$ can reach from $0.02m/s$ to $0.05m/s$ in the vicinity of the inner and outer banks under ice-covered condition. Such a magnitude is comparable to the bed shear stress under open-surface condition near the outer bank as shown in Figure 12 at a much higher level of flow discharge (Oa). This finding is rather surprising since the ice-covered flow discharge is much smaller in comparison to the open-surface ones as shown in Table 1. Such a sharp increase indicates a potential impact on sediment transport processes in shallow areas. Future efforts should be carried out to investigate this phenomenon further.

Overall, the friction method (2.6) provides an excellent estimation of $u_b^\star$ with minimal input information, especially at low discharge. Under low flow condition (Oc and Od) in Figure 12B, the friction method predicts that $u_b^\star \approx 0.007m/s$ where as the logarithmic method suggests that $u_b^\star \approx 0.01m/s$. However, the it cannot provide an accurate estimation of $u_b^\star$ at high discharge (Oa and Ob) as shown in Figure 12A. The friction method gives a reasonable estimation of $u_b^\star \approx 0.01m/s$ throughout the cross-section. However, it cannot capture the extreme values of $u_b^\star$ near the outer bank. Its limitation is further confirmed under ice-covered condition as displayed in Figure 13 as it is not able to capture the high shear velocity regions near banks. Our results in Figure 12 and Figure 13 show that the friction method can be used to provide an overall estimation of $u_b^\star$ in both open-surface and ice-covered conditions. However, a careful approach must be carried out to examine shear velocities near banks separately.

4.6 Limitation

In laboratory measurement or numerical simulation (Ma et al., 2021), turbulent statistics can be obtained by extending the averaging time T to an extremely large value ($T = 50\frac{H}{u_b^\star}$, for example). Under field conditions, it is challenging to obtain reliable data for the velocity profile (Biron et al., 1998) in large rivers. It is because of a well-known limitation of the ADCP signal near the river bed. It requires a long period of measurement (Petrie & Diplas, 2016) to provide an accurate time-averaged velocity profile. Therefore, the duration of measurement (Buffin-Bélanger & Roy, 2005) plays an important role in attaining statistically convergent results. Under open-surface condition, our time series length is set to be a minimum of $600s$ in all vertical locations. Note that the $T_\infty =$ 10 minutes has been reported to be sufficient for ADCP measurement (Chauvet et al., 2014) to reconstruct secondary flow features at field scale. The impacts of T_∞ on the reconstructed secondary flow velocity are examined in Figure 14. The time series at the vertical Oa_8 (the center of the main circulation) is also separated into four subsets with different periods $D-1$, $D-2$, $D-3$, and $D-4$ (see section 3.1). The structure of the main circulatory vortex is visible and consistent across all averaging periods ($D-1$, $D-2$, $D-3$, and $D-4$). In this case, the 10-minute records ensure that the three-dimensional flow structure is captured accurately.

Since the field campaign can be only carried out when the ice cover is sufficiently thick ($\geq 0.25m$) for this Red River, it thus requires that the air temperature in the field campaign should be sufficiently low (a typical situation in February). The ADCP M9 sensor can function properly in the range of air temperature ($> -20^0C$). However, a prolonged campaign in few hours in many ice holes leads to the deterioration of the signal quality as the sensor surface can become frozen easily and make a long acquisition infeasible. In contrast to the open-surface condition, the record length (T_∞) of our ice measurements is relatively short (2 minutes) to prevent the $M9$ sensor surface from freezing. Such a short duration (2 minutes) might not be enough to obtain the convergent profile $u_\infty(z)$. The impacts of the short period of averaging on the vertical profile are shown in Figure 15. Two measurements $M1$ and $M2$ are shown in the same Ib_7 ice hole.

It is evident that the exists a difference in the value of u_i^+ in the ice layer between the measurement $M1$ and $M2$. Referring to the Table 4, it is shown that $u_1^\star = 0.0269m/s$ ($M1$) and $u_2^\star = 0.0255m/s$ ($M2$). Moreover, the separation from logarithmic profile initiates at $h^+ \approx 10,251$ in the first measurement ($M1$), while it is $h^+ \approx 9,693$ in the second measurement ($M2$). This behavior is consistent with the convergence characteristics as shown in Figure 6 where the two measurements exhibit slightly different convergence profiles. A similar situation is also observed for the ice hole Ie_2 as shown in Table 4. Recognizing this limitation, we perform two measurements ($M1$ and $M2$) in the same ice hole to increase the data availability for Ia, Ib, and Ie. However, only one measurement is performed for ice holes in Ic and Id. Therefore, the secondary flows and shear velocity distribution Figure 11 and Figure 13 might be affected by the short averaging period $T_\infty = 120s$.

5 CONCLUSION

The impacts of ice coverage on velocity profiles in a river bend are investigated using Acoustic Doppler Current Profiler. The main goal is to evaluate the changes in the vertical velocity profiles as well as the secondary flow pattern as the ice coverage emerges in a river bend. In addition, the quartic method is examined as an alternative procedure to derive the bed shear velocity instead of using the classical logarithmic method. Our results show that the vertical flow profiles and the bed shear velocity are altered significantly under ice coverage. The following conclusions are made:

1. Our data support the existence of a universal logarithmic layer close to the river bed (within 20% of the local depth) in the thalweg of the bend under open-surface condition. In certain locations, the logarithmic layer can extend up to 50% of the total depth. In wall units, the theoretical bound (Equation 3) is well respected.
2. Under ice-covered condition, the logarithmic law is not recognized for the majority of the vertical locations. In the cases where it is applicable, the logarithmic layer is restricted in 20% of the total depth.
3. It might be challenging to use the logarithmic law to derive the shear velocities $u_b^\star$ and $u_i^\star$ due to the lack of data both temporally and spatially near the bed and the ice layers. On the other hand, the quartic solution (Guo et al., 2017) is helpful in determining these shear velocities. The quartic solution, however, is sensi-

tive to the determination of z_{max}, which might result in an underestimation of the shear stresses.

4. Our results show that the ice coverage changes the spatial distribution of the bed shear stress across the cross-section. Under the open-surface condition, the spatial distribution of bed shear velocity is skewed toward the outer bank, especially under a high discharge. Under the ice-covered condition, high values of bed shear velocity appear on both banks. The elevated values of shear stresses near the banks suggest that sediment transport processes might be active during winter in shallow areas.

6 OPEN RESEARCH

LiDAR Data from the State Water Commission of North Dakota (`https://lidar.dwr.nd.gov/`) were used in the creation of this manuscript. The hydrological data is extracted from the measurement data of the United States Geological Survey (USGS) station (USGS FARGO 09020104). Figures were made with Matplotlib version 3.2.1 (Caswell et al ,2020; Hunter, 2007), available under the Matplotlib license at `https://matplotlib.org/`. Velocity contours and vectors were created through the open-source Paraview software (5.4.1). The flow velocity data was first processed using the Velocity Mapping Toolbox (VMT) version (4.09) licensed, available at `https://hydroacoustics.usgs.gov/movingboat/VMT/VMT.shtml`. The raw data is processed with our MATLAB (v. 9.6) scripts. Our raw data is available at `https://github.com/trunglendsu/ESIP/tree/main/ADCP_Data`.

Acknowledgments

This work is mainly supported by a start-up package of Trung Le from North Dakota State University and a grant from ND EPSCoR Office FAR0032223. In addition, Berkay Koyuncu is supported by predoctoral fellowships from North Dakota Water Resources Research Institute and the Environmental Conservation Sciences program of NDSU. This work is also based on materials provided by the ESIP Lab with support from the National Aeronautics and Space Administration (NASA), National Oceanic and Atmospheric Administration (NOAA), and the United States Geologic Survey (USGS). We also acknowledge the use of computational resources at the Center for Computationally Assisted Science and Technology (CCAST)-NDSU and an allocation (CTS200012) from the Extreme Science and Engineering Discovery Environment (XSEDE), which is supported by National Science Foundation grant number ACI-1548562. We acknowledge the financial support of NSF RET - 1953102 to disseminate the findings of this study to local communities including the K-12 teachers in the City of Fargo and West Fargo, North Dakota.

We give special thanks to Dr. Xuefeng Chu (NDSU) for initiating our interest in ice hydraulics. We acknowledge the assistance of Daniel Thomas (USGS) and the Dakota Water Science Center in measuring and providing data for flows under ice coverage. We would like to thank Peter Goettsch and Christopher Broz (USGS) in helping us setting up the measurement configuration.

The authors declare no conflicts of interest.

References

Anwar, H. O. (1986). Turbulent structure in a river bend. *Journal of hydraulic engineering*, *112*(8), 657–669.

Attar, S., & Li, S. (2012). Data-fitted velocity profiles for ice-covered rivers. *Canadian Journal of Civil Engineering*, *39*(3), 334–338.

Attar, S., & Li, S. (2013). Momentum, energy and drag coefficients for ice-covered rivers. *River Research and Applications*, *29*(10), 1267–1276.

Bagherimiyab, F., & Lemmin, U. (2013). Shear velocity estimates in rough-bed open-channel flow. *Earth surface processes and landforms*, *38*(14), 1714–1724.

Bathurst, J. C., Hey, R. D., & Thorne, C. R. (1979). Secondary flow and shear stress at river bends. *Journal of the Hydraulics Division*, *105*(10), 1277–1295.

Beltaos, S., & Prowse, T. (2009). River-ice hydrology in a shrinking cryosphere. *Hydrological Processes: An International Journal*, *23*(1), 122–144.

Biron, P. M., Buffin-Bélanger, T., & Martel, N. (2019). Three-dimensional turbulent structures at a medium-sized confluence with and without an ice cover. *Earth Surface Processes and Landforms*, *44*(15), 3042–3056.

Biron, P. M., Lane, S. N., Roy, A. G., Bradbrook, K. F., & Richards, K. S. (1998). Sensitivity of bed shear stress estimated from vertical velocity profiles: The problem of sampling resolution. *Earth Surface Processes and Landforms: The Journal of the British Geomorphological Group*, *23*(2), 133–139.

Biron, P. M., Robson, C., Lapointe, M. F., & Gaskin, S. J. (2004). Comparing different methods of bed shear stress estimates in simple and complex flow fields. *Earth Surface Processes and Landforms: The Journal of the British Geomorphological Research Group*, *29*(11), 1403–1415.

Blanchard, R. A., Ellison, C. A., Galloway, J. M., & Evans, D. A. (2011). *Sediment concentrations, loads, and particle-size distributions in the red river of the north and selected tributaries near fargo, north dakota, during the 2010 spring high-flow event* (Tech. Rep.). U. S. Geological Survey.

Buffin-Bélanger, T., & Roy, A. G. (2005). 1 min in the life of a river: Selecting the optimal record length for the measurement of turbulence in fluvial boundary layers. *Geomorphology*, *68*(1-2), 77–94.

Chassiot, L., Lajeunesse, P., & Bernier, J.-F. (2020). Riverbank erosion in cold environments: Review and outlook. *Earth-Science Reviews*, *207*, 103231.

Chaudhry, M. H. (2007). *Open-channel flow.* Springer Science & Business Media.

Chauvet, H., Devauchelle, O., Métivier, F., Lajeunesse, E., & Limare, A. (2014). Recirculation cells in a wide channel. *Physics of Fluids*, *26*(1), 016604.

Chen, G., Gu, S., Li, B., Zhou, M., & Huai, W. (2018). Physically based coefficient for streamflow estimation in ice-covered channels. *Journal of hydrology*, *563*, 470–479.

Demers, S., Buffin-Bélanger, T., & Roy, A. (2011). Helical cell motions in a small ice-covered meander river reach. *River research and applications*, *27*(9), 1118–1125.

Engel, F. L., & Rhoads, B. L. (2016). Three-dimensional flow structure and patterns of bed shear stress in an evolving compound meander bend. *Earth Surface Processes and Landforms*, *41*(9), 1211–1226.

Ettema, R. (2002). Review of alluvial-channel responses to river ice. *Journal of Cold Regions Engineering*, *16*(4), 191–217.

Flack, K. A., & Schultz, M. P. (2010). Review of hydraulic roughness scales in the fully rough regime. *Journal of Fluids Engineering*, *132*(4).

Galloway, J. M., & Nustad, R. A. (2012). *Sediment loads in the red river of the north and selected tributaries near fargo, north dakota, 2010—2011* (Tech. Rep.). US Geological Survey.

Gao, W., Cheng, W., & Samtaney, R. (2020). Large-eddy simulations of turbulent flow in a channel with streamwise periodic constrictions. *Journal of Fluid Mechanics*, *900*.

Ghareh Aghaji Zare, S., Moore, S. A., Rennie, C. D., Seidou, O., Ahmari, H., & Malenchak, J. (2016). Estimation of composite hydraulic resistance in ice-covered alluvial streams. *Water Resources Research*, *52*(2), 1306–1327.

Guo, J. (2017). Eddy viscosity and complete log-law for turbulent pipe flow at high reynolds numbers. *Journal of Hydraulic Research*, *55*(1), 27–39.

Guo, J., Shan, H., Xu, H., Bai, Y., & Zhang, J. (2017). Exact solution for asymmetric turbulent channel flow with applications in ice-covered rivers. *Journal of Hydraulic Engineering*, *143*(10), 04017041.

Hanjalić, K., & Launder, B. (1972). Fully developed asymmetric flow in a plane channel. *Journal of Fluid Mechanics*, *51*(2), 301–335.

Hurther, D., & Lemmin, U. (2000). Shear stress statistics and wall similarity analysis in turbulent boundary layers using a high-resolution 3-d advp. *IEEE journal of oceanic engineering*, *25*(4), 446–457.

Kämäri, M., Alho, P., Veijalainen, N., Aaltonen, J., Huokuna, M., & Lotsari, E. (2015). River ice cover influence on sediment transportation at present and under projected hydroclimatic conditions. *Hydrological Processes*, *29*(22), 4738–4755.

Knoll, L. B., Sharma, S., Denfeld, B. A., Flaim, G., Hori, Y., Magnuson, J. J., ... Weyhenmeyer, G. A. (2019). Consequences of lake and river ice loss on cultural ecosystem services. *Limnology and Oceanography Letters*, *4*(5), 119–131.

Lau, Y. L., & Krishnappan, B. G. (1985). Sediment transport under ice cover. *Journal of Hydraulic Engineering*, *111*(6), 934–950.

Lauzon, R., Piliouras, A., & Rowland, J. C. (2019). Ice and permafrost effects on delta morphology and channel dynamics. *Geophysical Research Letters*, *46*(12), 6574–6582.

López, F., & García, M. H. (1999). Wall similarity in turbulent open-channel flow. *Journal of engineering mechanics*, *125*(7), 789–796.

Lotsari, E., Dietze, M., Kämäri, M., Alho, P., & Kasvi, E. (2020). Macro-turbulent flow and its impacts on sediment transport potential of a subarctic river during ice-covered and open-channel conditions. *Water*, *12*(7), 1874.

Lotsari, E., Kasvi, E., Kämäri, M., & Alho, P. (2017). The effects of ice cover on flow characteristics in a subarctic meandering river. *Earth Surface Processes and Landforms*, *42*(8), 1195–1212.

Ma, R., Alamé, K., & Mahesh, K. (2021). Direct numerical simulation of turbulent channel flow over random rough surfaces. *Journal of Fluid Mechanics*, *908*.

Marusic, I., Monty, J. P., Hultmark, M., & Smits, A. J. (2013). On the logarithmic region in wall turbulence. *Journal of Fluid Mechanics*, *716*.

Moradi, G., Vermeulen, B., Rennie, C. D., Cardot, R., & Lane, S. N. (2019). Evaluation of adcp processing options for secondary flow identification at river junctions. *Earth Surface Processes and Landforms*, *44*(14), 2903–2921.

Parker, G. (1991). Selective sorting and abrasion of river gravel. ii: Applications. *Journal of Hydraulic Engineering*, *117*(2), 150–171.

Parthasarathy, R., & Muste, M. (1994). Velocity measurements in asymmetric turbulent channel flows. *Journal of Hydraulic Engineering*, *120*(9), 1000–1020.

Peng, X., Zhang, T., Frauenfeld, O. W., Du, R., Jin, H., & Mu, C. (n.d.). A holistic assessment of 1979–2016 global cryospheric extent. *Earth's Future*, e2020EF001969.

Petrie, J., & Diplas, P. (2016). Evaluation of the logarithmic law of the wall for river flows. *River Research and Applications*, *32*(5), 1082–1093.

Petrie, J., Diplas, P., Gutierrez, M., & Nam, S. (2013). Data evaluation for acoustic doppler current profiler measurements obtained at fixed locations in a natural river. *Water Resources Research*, *49*(2), 1003–1016.

Prowse, T. D. (2001a). River-ice ecology. i: Hydrologic, geomorphic, and water-quality aspects. *Journal of Cold Regions Engineering*, *15*(1), 1–16.

Prowse, T. D. (2001b). River-ice ecology. ii: Biological aspects. *Journal of Cold Regions Engineering*, *15*(1), 17–33.

Shen, C., & Lemmin, U. (1997). A two-dimensional acoustic sediment flux profiler. *Measurement Science and Technology*, *8*(8), 880.

Smith, B. T., & Ettema, R. (1995). *Ice-cover influence on flow and bedload transport in dune-bed channels.* Iowa Institute of Hydraulic Research, the University of Iowa.

Soulsby, R. (1981). Measurements of the reynolds stress components close to a marine sand bank. *Marine Geology*, *42*(1-4), 35–47.

Stoesser, T., Ruether, N., & Olsen, N. R. B. (2010). Calculation of primary and secondary flow and boundary shear stresses in a meandering channel. *Advances in Water Resources*, *33*(2), 158–170.

Stone, M. C., & Hotchkiss, R. H. (2007). Evaluating velocity measurement techniques in shallow streams. *Journal of Hydraulic Research*, *45*(6), 752–762.

Sukhodolov, A., Thiele, M., Bungartz, H., & Engelhardt, C. (1999). Turbulence structure in an ice-covered, sand-bed river. *Water resources research*, *35*(3), 889–894.

Sukhodolov, A. N. (2012). Structure of turbulent flow in a meander bend of a lowland river. *Water Resources Research*, *48*(1).

Tatinclaux, J.-C., & Gogus, M. (1983). Asymmetric plane flow with application to ice jams. *Journal of Hydraulic Engineering*, *109*(11), 1540–1554.

Thellman, A., Jankowski, K. J., Hayden, B., Yang, X., Dolan, W., Smits, A. P., & O'Sullivan, A. M. (2021). The ecology of river ice. *Journal of Geophysical*

Research: Biogeosciences, *126*(9), e2021JG006275.

Tsai, W.-F., & Ettema, R. (1994). Modified eddy viscosity model in fully developed asymmetric channel flows. *Journal of engineering mechanics*, *120*(4), 720–732.

Turcotte, B., Morse, B., Bergeron, N. E., & Roy, A. G. (2011). Sediment transport in ice-affected rivers. *Journal of hydrology*, *409*(1-2), 561–577.

Urroz, G. E., & Ettema, R. (1994a). Application of two-layer hypothesis to fully developed flow in ice-covered curved channels. *Canadian journal of civil engineering*, *21*(1), 101–110.

Urroz, G. E., & Ettema, R. (1994b). Small-scale experiments on ice-jam initiation in a curved channel. *Canadian Journal of Civil Engineering*, *21*(5), 719–727.

Volino, R. J., & Schultz, M. P. (2018). Determination of wall shear stress from mean velocity and reynolds shear stress profiles. *Physical Review Fluids*, *3*(3), 034606.

Wang, F., Huai, W., Liu, M., & Fu, X. (2020). Modeling depth-averaged streamwise velocity in straight trapezoidal compound channels with ice cover. *Journal of Hydrology*, *585*, 124336.

Wang, J., Sui, J.-y., & Karney, B. W. (2008). Incipient motion of non-cohesive sediment under ice cover—an experimental study. *Journal of Hydrodynamics*, *20*(1), 117–124.

Whiting, P. J., & Dietrich, W. E. (1990). Boundary shear stress and roughness over mobile alluvial beds. *Journal of Hydraulic Engineering*, *116*(12), 1495–1511.

Wilcock, P. R. (1996). Estimating local bed shear stress from velocity observations. *Water Resources Research*, *32*(11), 3361–3366.

Yang, X., Pavelsky, T. M., & Allen, G. H. (2020). The past and future of global river ice. *Nature*, *577*(7788), 69–73.

Table 1. Expeditions in Fall 2020, Winter 2020 and 2021, and Summer 2021. The hydrological data (flow discharge Q and elevation) is monitored at the USGS Fargo (09020104) Station. The exact location of each vertical location is illustrated in Figure 10. T_{∞} (minutes) is the total time of measurement in each vertical/(ice hole) location. The notations $M1$ and $M2$ denote two consecutive measurements in one ice hole.

Case	*Date*	*Surface*	Q (m^3/s)	Elevation (m)	No. verticals	T_{∞} (mins)
Oa	Oct/02/20	open	23.41	265.96	13	10
Ob	Oct/04/20	open	23.87	265.96	12	10
Oc	June/22/21	open	14.30	265.87	8	15
Od	June/24/21	open	12.20	265.85	11	15
Oe	June/30/21	open	6.82	265.72	6	15
Ia (M1/M2)	Feb/19/21	ice	12.5	265.92	6	2
Ib (M1/M2)	Feb/20/21	ice	12.8	265.92	7	2
Ic	Feb/21/21	ice	13.8	265.93	7	2
Id	Feb/21/21	ice	13.8	265.93	8	2
Ie (M1/M2)	Feb/21/21	ice	13.8	265.93	6	2

Table 2. Derivation of the shear velocity $u_b^\star$ and the equivalent roughness height (z_0) using the logarithmic fitting (section 2.4) for the case Oa, Ob, Oc, Od, and Oe (see Table 1). The friction Reynolds number Re_τ^b and the thickness of the logarithmic layer δ_b^+ are explained in Equation 1. The theoretical bound for δ_{theory}^+ is computed from Equation 3. Only the stations in the thalweg region ($H \geq 3.5m$) are listed in this table.

Case	$H(m)$	$\frac{\delta_b}{H}$	R^2	$u_b^\star$ (m/s)	z_0 (m)	Re_τ	δ_b^+	δ_{theory}^+
Oa_4	3.66	0.50	0.99	0.0150	0.061	57,876	28,938	8681
Oa_5	4.10	0.50	0.94	0.0136	0.0245	55,883	27,941	8382
Oa_{10}	3.83	0.50	0.95	0.0090	0.014	34,453	17,226	5168
Ob_5	4.10	0.50	0.91	0.0087	0.0003	35,549	17,774	5332
Ob_6	4.20	0.30	0.95	0.0079	1.5×10^{-4}	24,613	7,384	3692
Ob_7	4.23	0.20	0.99	0.0095	9.7799	57,067	11,413	8560
Ob_8	3.99	0.20	0.99	0.0125	0.0365	12,428	2,485	1864
Ob_9	3.82	0.20	0.98	0.0124	0.1006	27,596	5,519	4139
Oc_2	3.50	0.50	0.99	0.0069	0.0089	24,147	12,073	1811
Oc_4	3.95	0.35	0.99	0.0070	0.0188	32,142	11,249	4821
Oc_5	4.06	0.20	0.99	0.00796	0.0195	26,764	5,352	4015
Oc_6	3.95	0.50	0.98	0.01557	0.4489	61,531	30,765	9230
Oc_7	3.65	0.45	0.97	0.0121	0.4760	46,680	21,006	7002
Od_3	3.64	0.50	0.99	0.0122	0.5166	44,313	22,156	3323
Od_4	3.88	0.40	0.98	0.0078	0.4182	33,176	13,270	4976
Od_5	4.09	0.50	0.96	0.0121	0.5056	49,544	24,772	7431
Od_6	4.22	0.40	0.97	0.0107	0.4165	51,227	20,491	7684
Od_7	4.10	0.50	0.98	0.0109	0.2300	44,573	22,286	6686
Od_8	3.80	0.50	0.96	0.0089	0.0570	33,914	16,957	5087
Od_9	3.60	0.50	0.93	0.0096	0.2257	34,722	17,361	5208
Od_{10}	3.70	0.45	0.99	0.0131	1.2623	49,931	22,469	7490
Oe_2	4.01	0.50	0.94	0.0124	2.0462	49,601	24,800	7440
Oe_3	4.03	0.35	0.98	0.0088	1.1045	43,687	15,290	6595
Oe_4	4.05	0.45	0.96	0.0110	2.2522	47,432	21,344	7115
Oe_5	3.76	0.50	0.94	0.0089	0.6461	33,410	16,705	5011

Table 3. Derivation of the shear velocity $u_b^\star$ and the equivalent roughness height (z_0) using the logarithmic fitting (section 2.4) for the case Ia, Ib, Ic, and Id (see Table 1). The friction Reynolds number Re_τ and the thickness of the logarithmic layer δ_b^+ are explained in Equation 1. The theoretical bound for δ_{theory}^+ is computed from Equation 3.

Case	H (m)	$\frac{\delta_b}{H}$	R^2	$u_b^\star$ (m/s)	z_0 (m)	Re_τ	δ_b^+	δ_{theory}^+
Ia_6	1.93	0.40	0.9734	0.0161	1.8574	31.088	13.990	4663
Ib_2	3.11	0.50	0.9158	0.0128	0.1205	40,001	16,000	6000
Ib_6	2.60	0.35	0.9418	0.0137	0.1364	35,623	8,905	5343
$Ib_7(M_1)$	2.33	0.50	0.9472	0.0352	5.5386	82,102	28,736	12315
$Ib_7(M_2)$	2.33	0.50	0.9478	0.0477	5.6604	111,125	38,893	16669
Ic_2	3.50	0.50	0.9162	0.0102	0.0538	29,113	14,556	4367
Id_2	3.43	0.50	0.9620	0.0170	0.998	47,217	23,608	7083
Id_6	3.42	0.50	0.9206	0.0089	0.0247	24,773	12,386	3716
Id_8	1.65	0.45	0.9921	0.0203	1.5292	26,143	11,764	3921

Table 4. Derivation of the shear velocity $u_i^\star$ and the equivalent roughness height (z_0) using the logarithmic fitting (section 2.4) for the case Ia, Ib, Ic, and Id (see Table 1). The friction Reynolds number Re_τ^i and the thickness of the logarithmic layer δ_i^+ are explained in Equation 1. The theoretical bound for δ_{theory}^+ is computed from Equation 3.

Case	H (m)	$\frac{\delta_i}{H}$	R^2	$u_i^\star$ (m/s)	z_0 (m)	Re_τ	δ_i^+	δ_{theory}^+
Ia_1	1.72	0.30	0.9033	0.0213	2.0291	29,706	8,912	4455
Ia_4	3.46	0.20	0.9499	0.0117	0.0767	33,374	6,675	5006
Ia_5	3.39	0.30	0.9276	0.0197	0.7907	27,459	8,238	4118
Ib_4	4.01	0.20	0.9174	0.0083	0.0007	27,177	5,435	4076
Ib_5	3.68	0.30	0.9837	0.0078	0.0023	23,455	7,037	3518
$Ib_7(M_1)$	2.33	0.20	0.9321	0.0269	0.6904	51,255	10,251	7688
$Ib_7(M_2)$	2.33	0.20	0.9921	0.0255	0.4402	48,465	9,693	7269
Ic_1	3.04	0.25	0.9262	0.0120	0.4061	30,021	7,505	4503
Ic_3	3.74	0.20	0.9398	0.0066	0.0001	21,242	4,248	3186
Ic_5	3.48	0.35	0.9630	0.0053	0.0001	15,101	5,285	2265
Id_2	3.43	0.25	0.9852	0.0089	0.0117	24,838	6,209	3725
Id_3	3.57	0.20	0.9404	0.0041	1×10^{-7}	11,917	2,383	1787
Id_5	3.74	0.30	0.9716	0.0053	1×10^{-5}	15,978	4,793	2396
Id_6	3.42	0.25	0.9663	0.0070	0.0011	19,543	4,886	2931
Id_8	1.65	0.30	0.9845	0.0049	0.0001	6,591	1,977	988
$Ie_2(M_1)$	2.39	0.20	0.9794	0.0067	0.0032	13,222	2,644	1983
$Ie_2(M_2)$	2.54	0.30	0.9860	0.0101	0.0392	20,941	6,282	3141
Ie_5	4.41	0.40	0.9322	0.0044	0.0001	15,930	6,372	2389
Ie_7	3.04	0.20	0.9539	0.0034	4.5×10^{-5}	8,313	1,662	1246

Table 5. Derivation of the shear velocity on the ice layer ($u_i^\star$) and the bed layer ($u_b^\star$) using the quartic solution (section 3.4) for the case Ia, Ib, Ic, and Id (see Table 1). The local Reynolds number based on shear velocity $u_b^\star$ and water viscosity ν is $Re_\tau = (Hu_b^\star)/\nu$. The location ($\eta_{max}$) and the maximum velocity (u_{max}) are determined by the iterative procedure in section 3.4.

Measurement	H (m)	$u_{max}(m/s)$	R^2	$u_b^\star$ (m/s)	$u_i^\star$ (m/s)	λ	η_{max}
Ia_2	3.14	0.1451	0.9184	0.0012	0.0016	1.3234	0.7269
Ia_5	3.39	0.1357	0.9273	0.0073	0.0032	0.4422	1.6729
Ib_2	3.11	0.1998	0.9916	0.0078	0.0062	0.7886	1.2331
Ib_4	4.01	0.2115	0.9748	0.0074	0.0048	0.6428	1.4153
Ib_5	3.70	0.1747	0.9846	0.0074	0.0049	0.6564	1.3977
Ib_6	2.60	0.1599	0.9795	0.0023	0.0030	1.3067	0.7387
Ib_7	2.33	0.2036	0.9828	0.0293	0.0193	0.6596	1.3937
Ic_2	3.50	0.1926	0.9746	0.0071	0.0034	0.4825	1.6223
Ic_4	3.95	0.1917	0.9765	0.0045	0.0034	0.7535	1.2756
Ic_5	3.48	0.1844	0.9383	0.0064	0.0050	0.7784	1.2454
Id_2	3.43	0.1846	0.9119	0.0143	0.0097	0.6777	1.3706
Id_3	3.57	0.1983	0.9560	0.0075	0.0033	0.4372	1.6791
Id_4	3.95	0.2023	0.9733	0.0060	0.0023	0.3879	1.7384
Id_5	3.74	0.1934	0.9812	0.0057	0.0035	0.6142	1.4521
Id_6	3.42	0.1843	0.9295	0.0084	0.0066	0.7912	1.2300
Id_7	2.84	0.1707	0.9254	0.0103	0.0046	0.4453	1.6690
Id_8	1.65	0.1476	0.9380	0.0121	0.0076	0.6305	1.4310
Ie_1	0.65	0.0839	0.9486	0.0022	0.0020	0.9009	1.1040
Ie_2	2.54	0.1551	0.9631	0.0088	0.0064	0.7290	1.3059
Ie_3	3.78	0.1741	0.9781	0.0056	0.0033	0.5836	1.4919
Ie_4	4.46	0.1596	0.9485	0.0044	0.0021	0.4776	1.6285
Ie_7	3.04	0.1094	0.9560	0.0063	0.0035	0.5624	1.5194

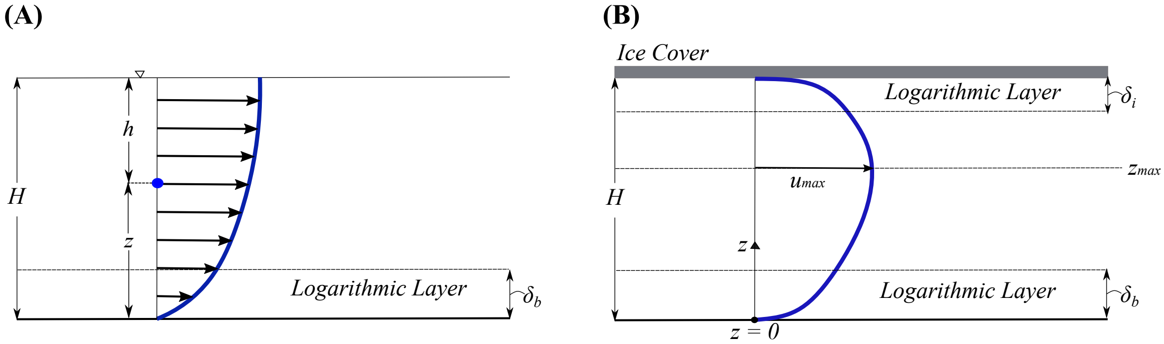

Figure 1. The differences in flow configuration under: (A) open surface condition, and (B) ice-covered condition. Under open-surface condition, the total depth $H = h + z$ is separated into two portions: i) the distance to the river bed (z) of a measured point; and ii) its local depth (h). The logarithmic layer is assumed to extend from the river bet at a distance δ_b. Under ice-covered condition, two logarithmic layers are assumed (two-layer hypothesis) near the ice layer (δ_i) and the river bed (δ_b). The z_{max} is the position of the maximum velocity (u_{max}) from the river bed.

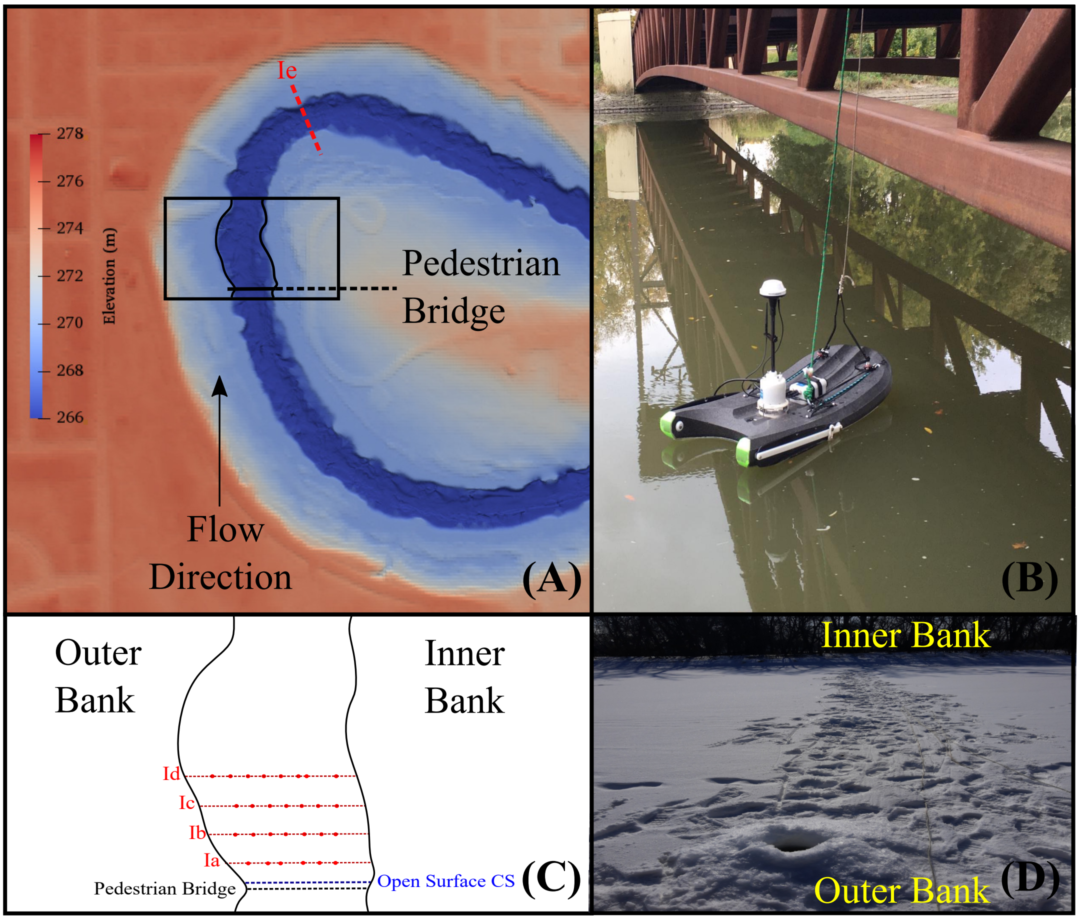

Figure 2. The study area and the measurement cross-sections. **(A)** The area of interest locates at the apex of a bend in the Red River, Fargo, North Dakota, the United States. The flow is in the North direction (bottom to top). The Digital Terrain Model (DTM) is generated from the North Dakota LiDar data (see section 6) and our bathymetry (ADCP) data. **(B)** Under open-surface condition, the ADCP M9 sensor is deployed a long a pedestrian bridge with the fixed-vessel methodology in five measurement days *Oa*, *Ob*, *Oc*, *Od*, and *Oe* (see Table 1). In each measurement day, the $M9$ is stationed in a number of vertical locations across the bridge as shown in Table 1. **(C)** The diagram shows the ice holes in five consecutive cross-sections Ia, Ib, Ic,Id and Ie in Feb/2021. Each cross-section (Ia, Ib, Ic, or Id) is separated from the adjacent one at a distance of 6.1m. The cross-section Ie locates at 310m downstream from the pedestrian bridge in (A). The number of ice holes for each cross-section is shown in Table 1. Each vertical location in one cross-section is marked by its distance from the corresponding left bank ℓ(m) (see also Figure 3).

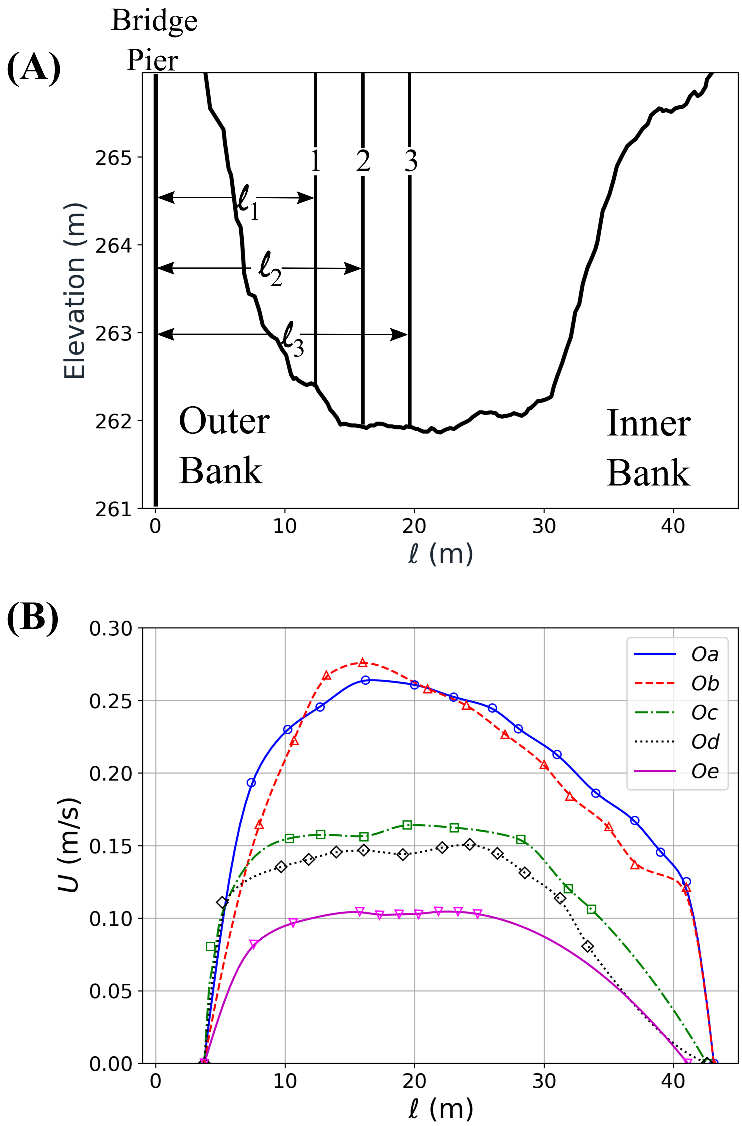

Figure 3. The depth-averaged velocity profiles (U) under open-surface condition at the bend apex. (A) The cross-section shape at the bridge. The value ℓ denotes the distance of the vertical location to the left bank. (B) Depth-averaged velocity profiles under different flow discharge Oa, Ob, Oc, Od, and Oe. The flow distribution is skewed toward the outer (left) bank. The thalweg is defined as area with the total depth $H \geq 3.5m$, which is in the $10m \leq \ell \leq 30m$ region for this cross-section. The measurement details are described in the Table 1.

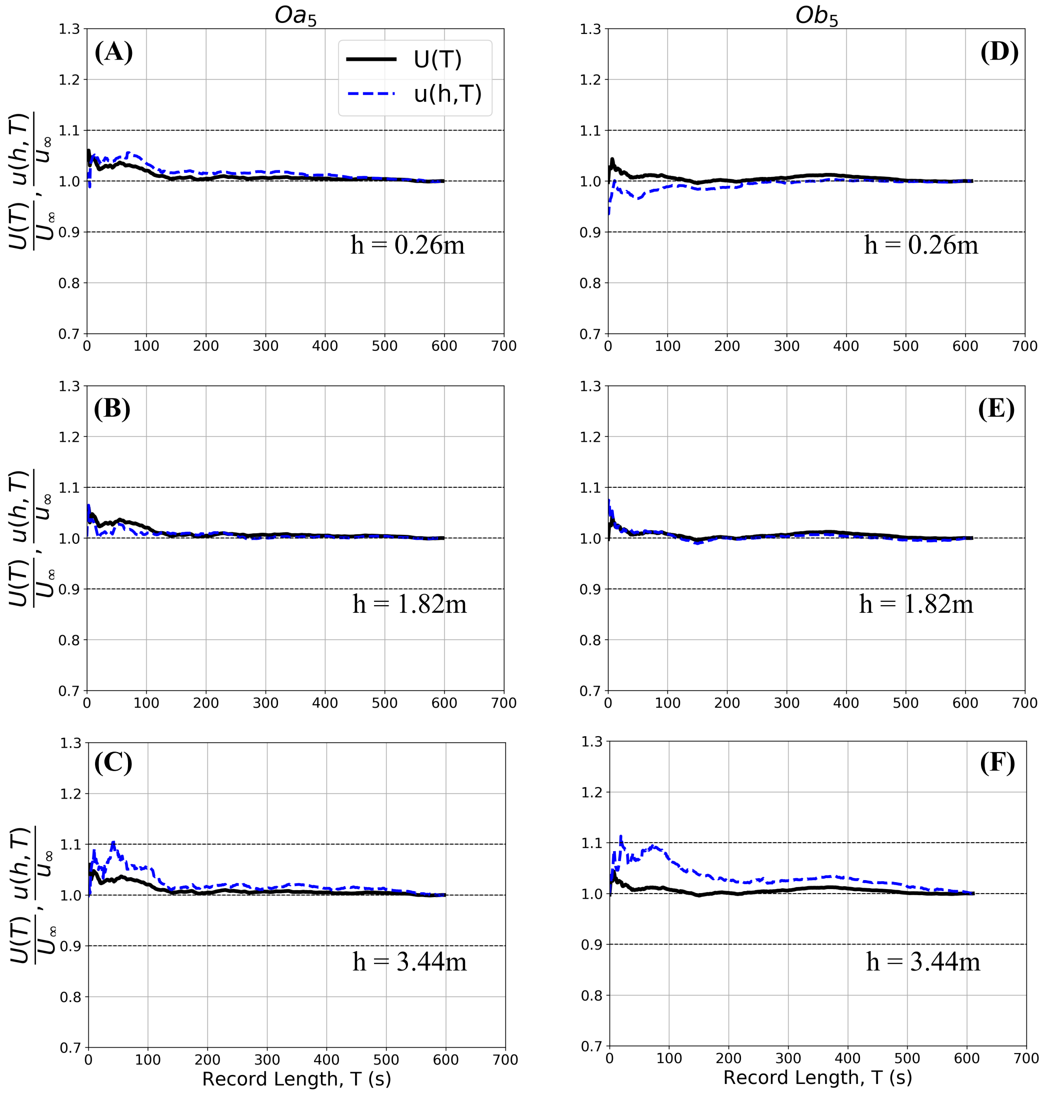

Figure 4. Statistical convergence properties for the depth-averaged velocity $U(T)$ and the time-averaged velocity $u(h,T)$ (section 2.3) as the function of the record length T for the vertical location Oa_5 (left column - $H_{Oa_5} = 4.1m$) and Ob_5 (right column - $H_{Ob_5} = 4.1m$). The record length T is varied from 1 second to the entire record ($T_\infty \approx 600s$). The long-term values of $U(T_\infty)$ and $u(h,T_\infty)$ are denoted as U_∞ and $u_\infty(h)$, respectively. Three values of depth are chosen $h = 0.26m$ (near surface), $h = 1.82m$ (mid-depth), and $h = 3.44m$ (near bed).

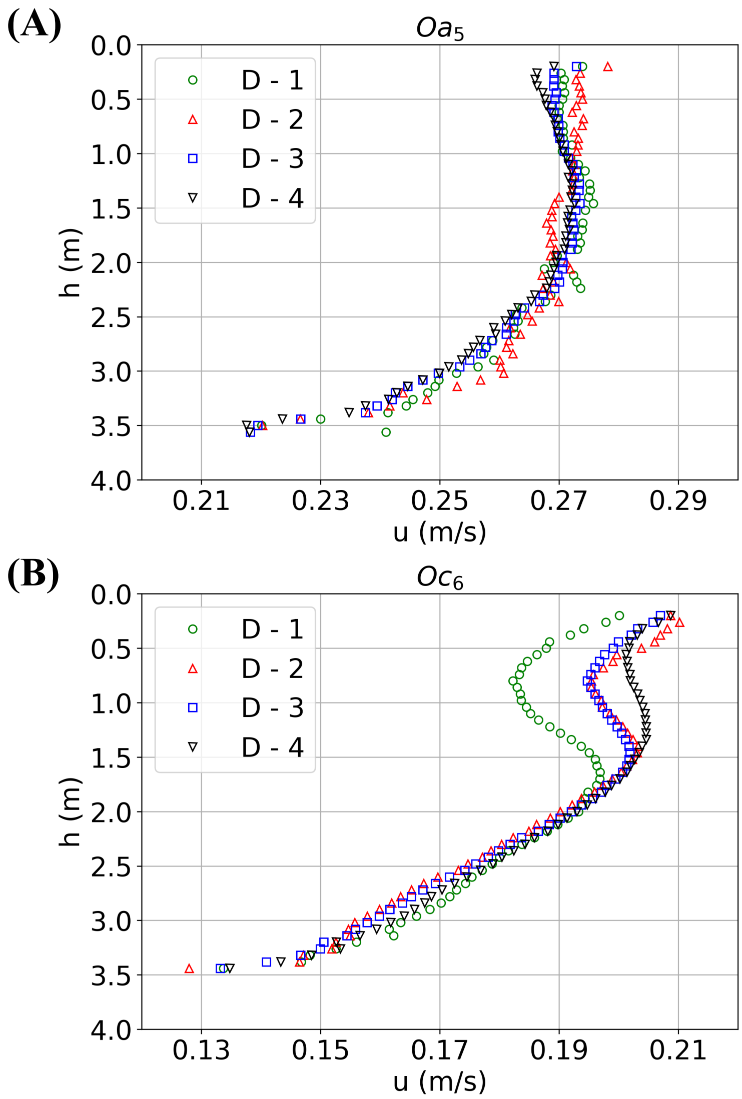

Figure 5. The variability of the vertical flow profile as the record length T changes at the vertical location Oc_6 and Od_5. Four periods ($D-1$, $D-2$, $D-3$, and $D-4$) with different values of measurement period T (seconds) are examined: $D-1$ ($t = 0 \rightarrow 120$ seconds); $D-2$ $t = 200 \rightarrow 320$ seconds; $D-3$ ($t = 0 \rightarrow 400$ seconds; and ($D-4$) $t = 0 \rightarrow 620$ seconds. The vertical flow profile near the river bed converges rapidly in the first 120 seconds.

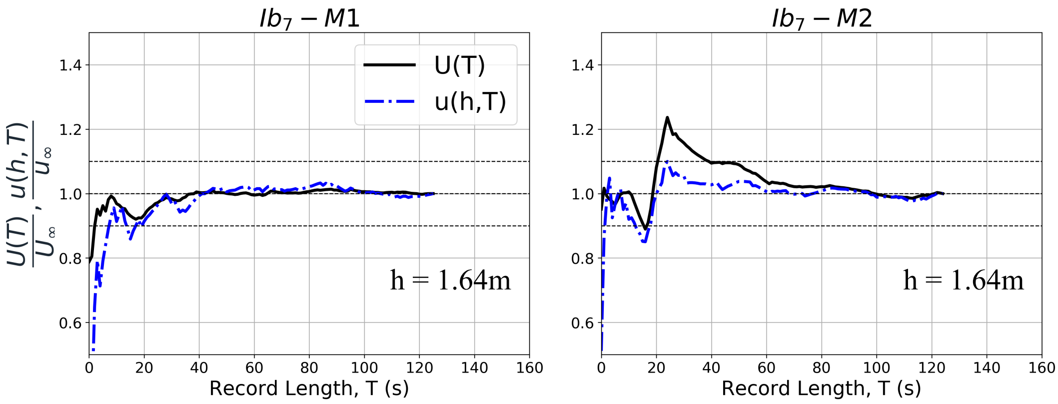

Figure 6. Statistical properties of the depth-averaged velocity $U(T)$ and the time-averaged velocity $u(h,T)$ under ice-covered condition as the function of the record length $T(s)$. Two measurements ($M1$ and $M2$) of same station Ib_7 are shown at the depth $h = 1.64m$. Here the sample length T is varied from 1 second to the entire record ($T_\infty = 120$ seconds). The long-term values of $U(T_\infty)$ and $u(h,T_\infty)$ are denoted as U_∞ and $u_\infty(h)$, respectively.

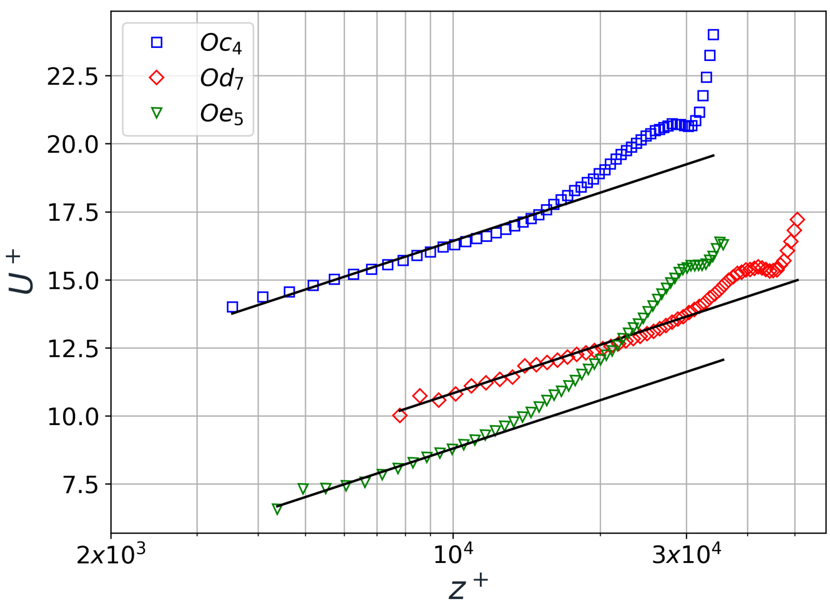

Figure 7. The presence of the logarithmic law (solid lines) at three vertical locations Oc_4 (blue circle), Od_7 (green triangle), Oe_5(red diamond) under open-surface condition (see Table 1). The logarithmic law (Equation 6) is written in wall units (see Equation 1). The separation from the logarithmic law determines the value of the logarithmic layer thickness δ_b^+. The logarithmic layer is considered as a collection of measured points near the river bed so that the value fitting of $R^2 \geq 0.9$ (see section 2.4).

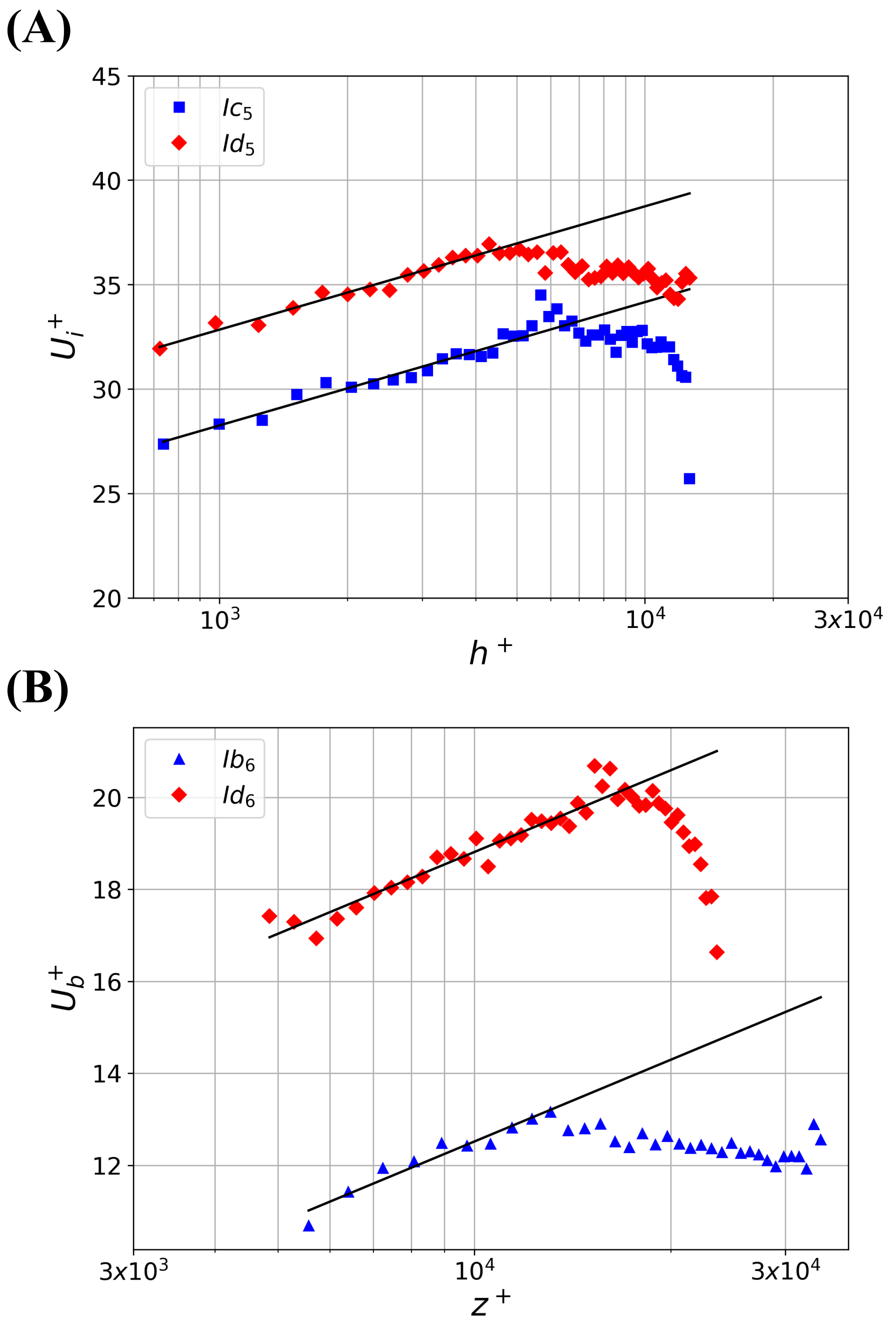

Figure 8. The presence of the logarithmic profile (solid lines) under ice-covered flows. (**A**) on the ice layer at the verticals Ic_5 (red circles) and Id_5 (blue triangles); and (**B**)on the bed layer at the verticals Ib_6 (blue triangle) and Id_6 (red circles). The logarithmic law (Equation 6) is written in wall units (see Equation 1 and Equation 2). The separation from the logarithmic law determines the value of the logarithmic layer thickness δ_i^+ and δ_b^+. The logarithmic layer is considered as a collection of measured points near the river bed so that the fitting value of $R^2 \geq 0.9$ (see section 2.4).

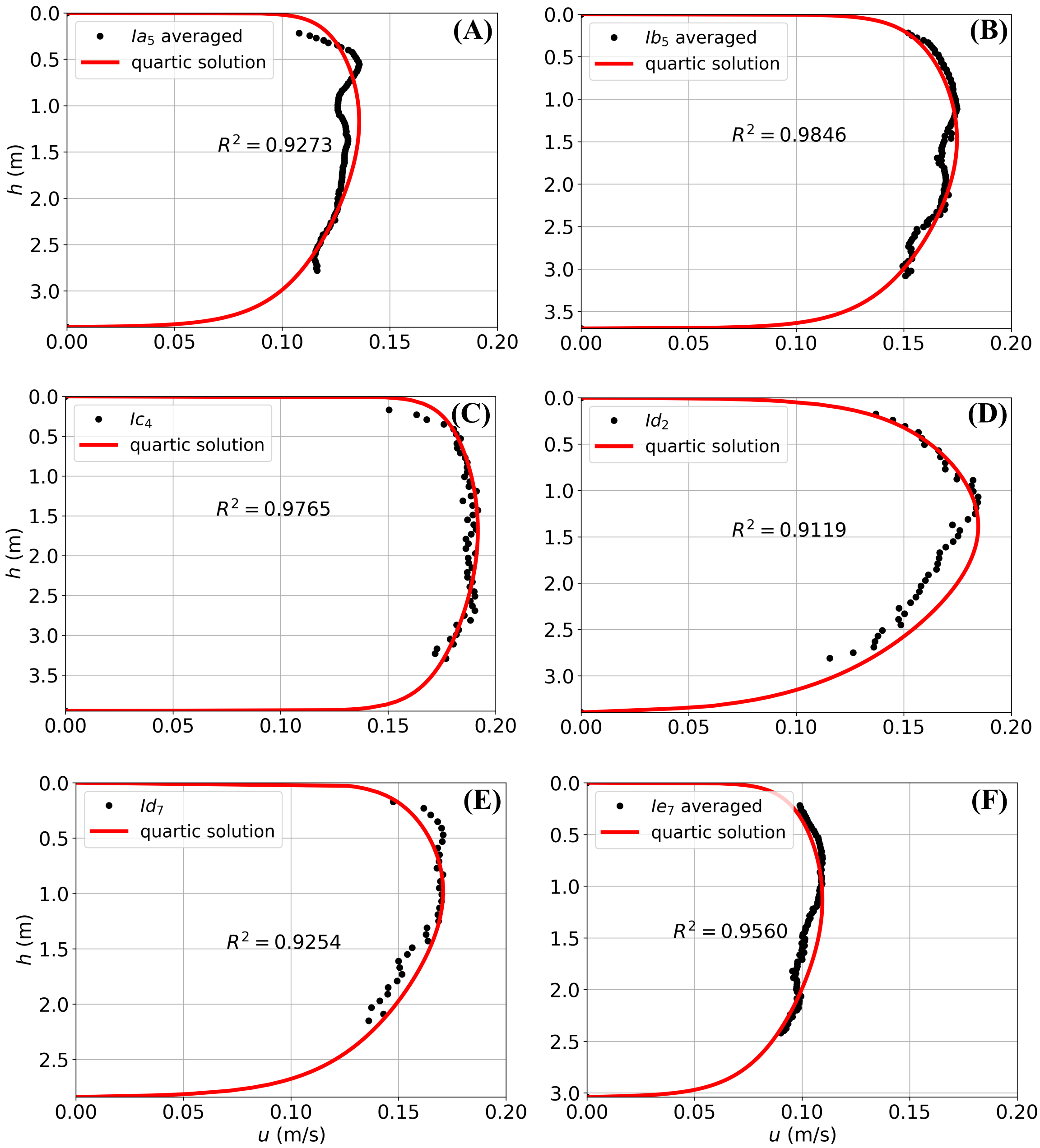

Figure 9. The agreement between the measured profiles and the quartic solution. The fitting procedure provides the shear velocity on the river bed ($u_b^\star$) and the ice layer ($u_i^\star$) in section 2.5. The details of the available data are described in Table 5 for all ice holes. The Signal-To-Noise Ratio (SNR) limits the data availability near the river bed and the ice layers. The averaged profile (from two measurements M1 and M2) is used for the cross-sections Ia, Ib, and Ie.

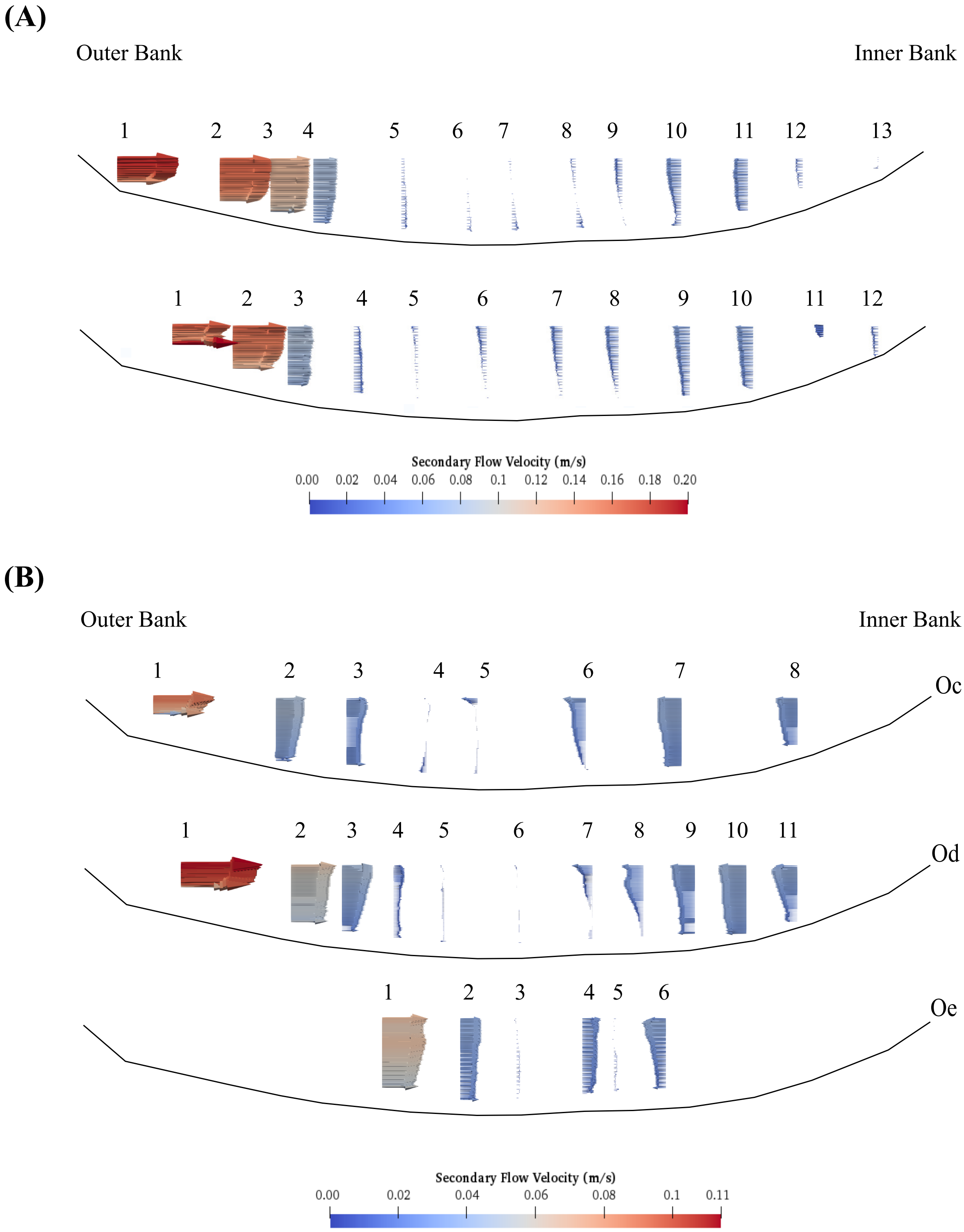

Figure 10. The dependence of secondary flow structures at the bridge cross-section on flow discharge (See Table 1) under open-surface condition. The secondary flow vectors are visualized using the time-averaged East (u_x) and Up (u_z) velocity components. All measurements (Oa, Ob, Oc, Od, and Oe) are conducted on the same cross-section (bridge location). The vertical location of each ADCP measurement on the cross-section is marked with numbers. The total number of the vertical locations for each measurement is summarized in Table 1.

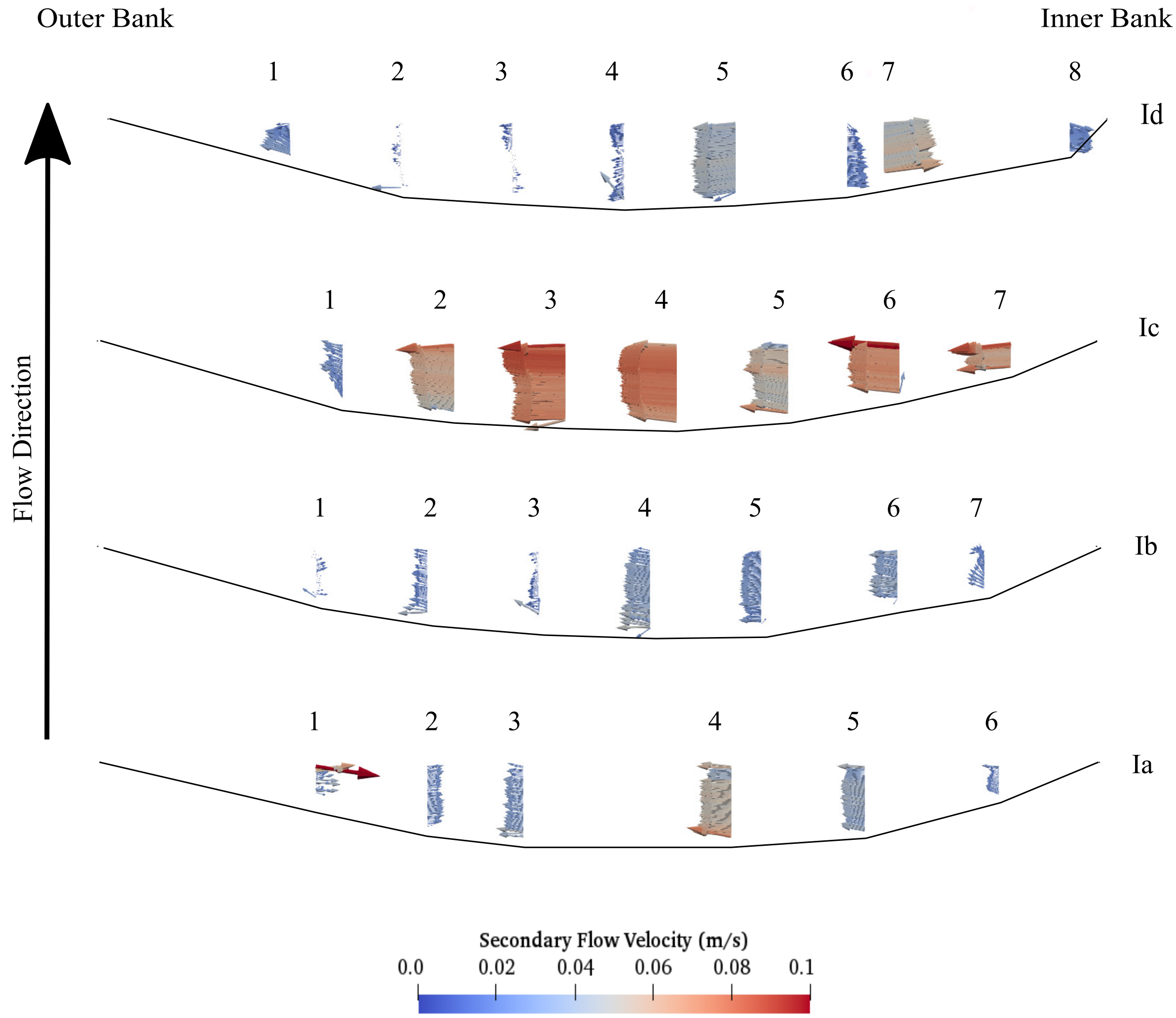

Figure 11. The spatial variability of secondary flow structures across four consecutive cross-sections under ice-covered condition in Feb/2021. The cross-sections Ia, Ib, Ic, and Id are parallel to each other and separated by a distance of $6.1m$ as shown in Figure 10. The flow direction is from Ia to Id in the South-North direction (bottom to top). The ice holes are numbered from the outer bank to the inner bank as shown in Table 1. The black arrows indicate the main circulatory pattern.

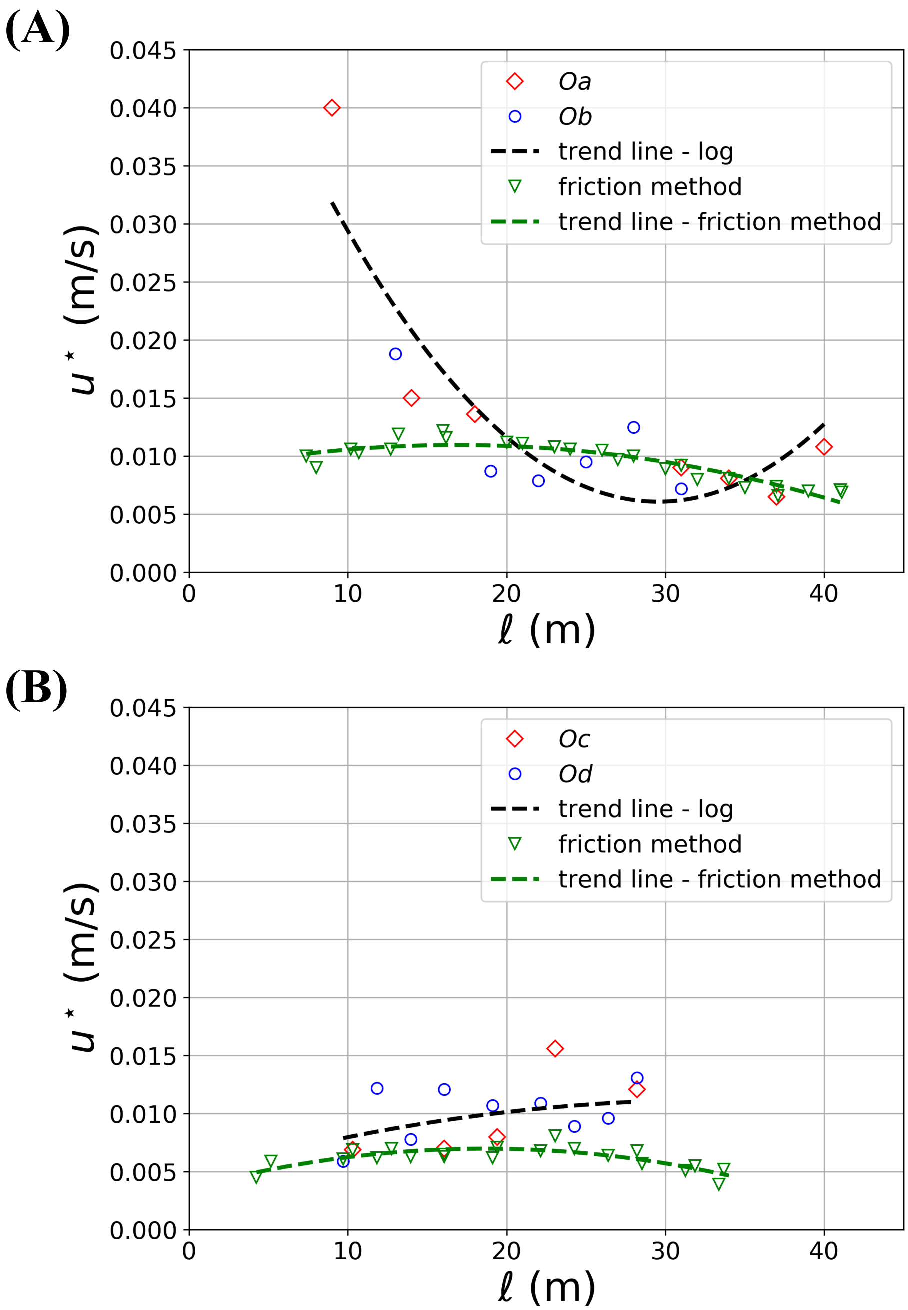

Figure 12. Shear velocity ($u_b^\star$) profiles on the river bed under open surface condition. The value of $u_b^\star$ is derived by the logarithmic fitting method in section 2.4. The relative location ℓ to the outer bank (along the East direction) is chosen to represent the vertical locations (see Figure 3). In the vicinity of the outer bank ($0 < \ell < 20m$), the value of $u_b^\star$ can reach up to $0.04m/s$. However, $u_b^\star$ reduces to the value $0.01m/s$ near the inner bank ($30 < \ell < 45m$). Two levels of flow discharge are examined: (**A**) high discharge ($Q_{Oa} = 23.41m^3/s$ and $Q_{Ob} = 23.87m^3/s$); and (**B**) low discharge ($Q_{Oc} = 14.3m^3/s$, $Q_{Od} = 12.2m^3/s$, and $Q_{Oe} = 6.82m^3/s$). The details of the flow measurements are reported in Table 1.

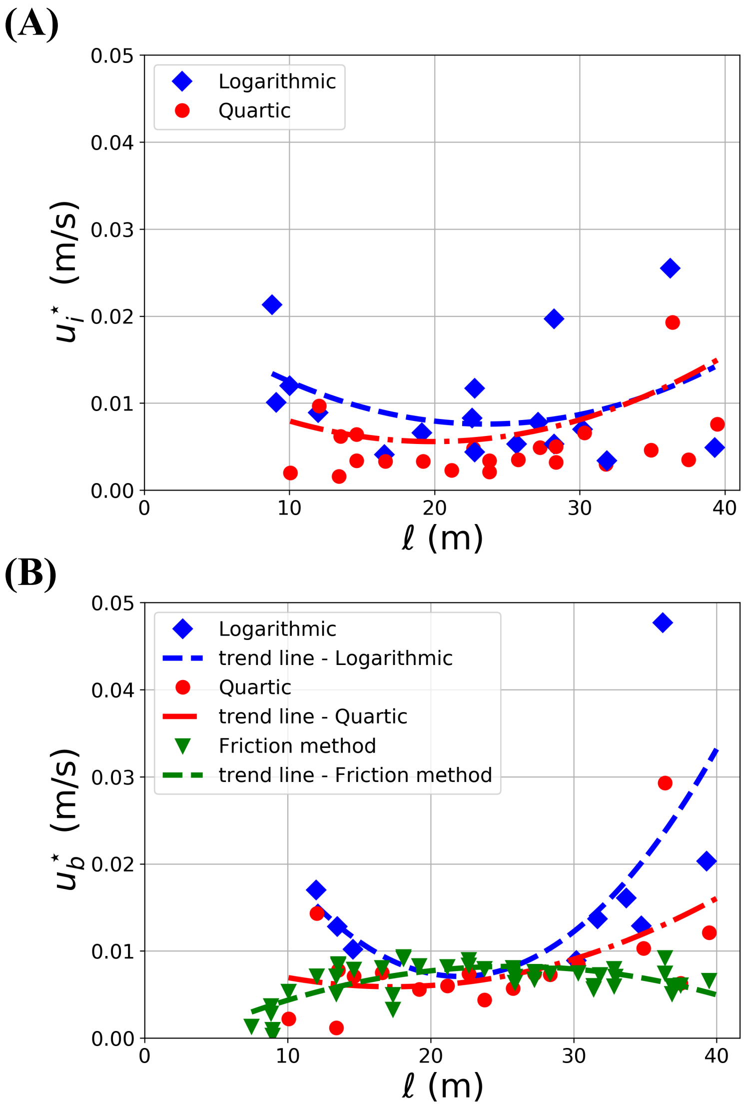

Figure 13. The distribution of shear velocity on: (**A**) the ice layer ($u_i^\star$), and (**B**) the river bed ($u_b^\star$) across the bend apex cross-section (see Figure 3, for the definition of ℓ). The filled symbols represent the shear velocities which are derived from the logarithmic methodology (section 2.4). The empty symbols represent the shear velocities, which are derived from the quartic methodology. The dash-dotted lines show the trend lines of $u_i^\star$ and $u_b^\star$ with each type of fitting methodology. The trend line is created using the MATLAB function, "*(*polyfit)", with the second degree.

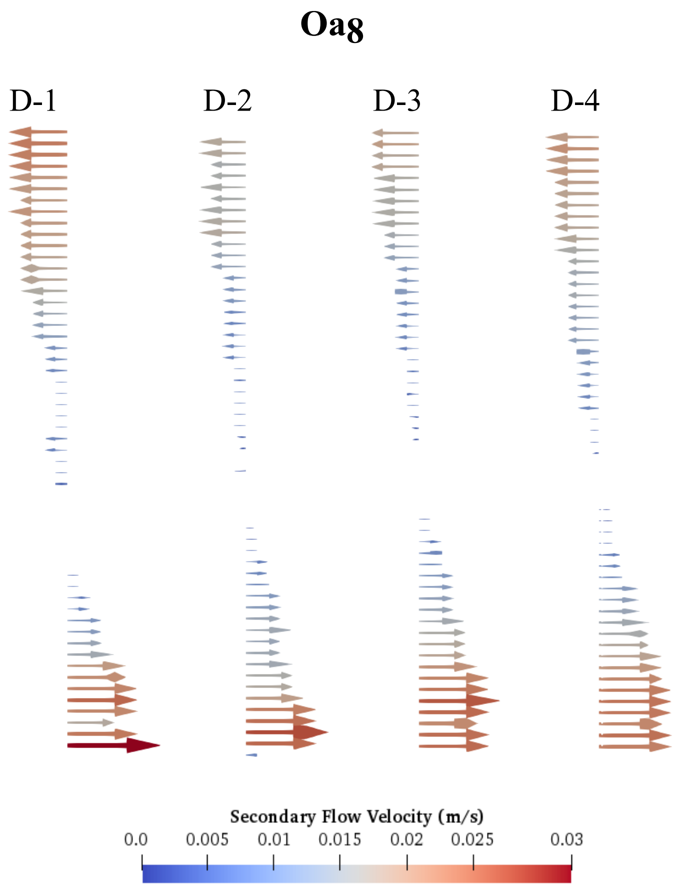

Figure 14. The sensitivity of the secondary flow velocities ($u_e(T_\infty)$, $u_z(T_\infty)$) to the length of the averaging period T (section 3.1). The structure of the secondary flow patterns are consistent across different scenarios of: (D_1) $t = 0 \rightarrow 120s$ ($T = 120s$; (D_2) $t = 200 \rightarrow 320s$ ($T = 120s$); (D_3) $t = 0 \rightarrow 400s$ ($T = 400s$); and (D_4) $t = 0 \rightarrow 620s$ ($T = 620s$). The center of the rotation is found closer to the bed.

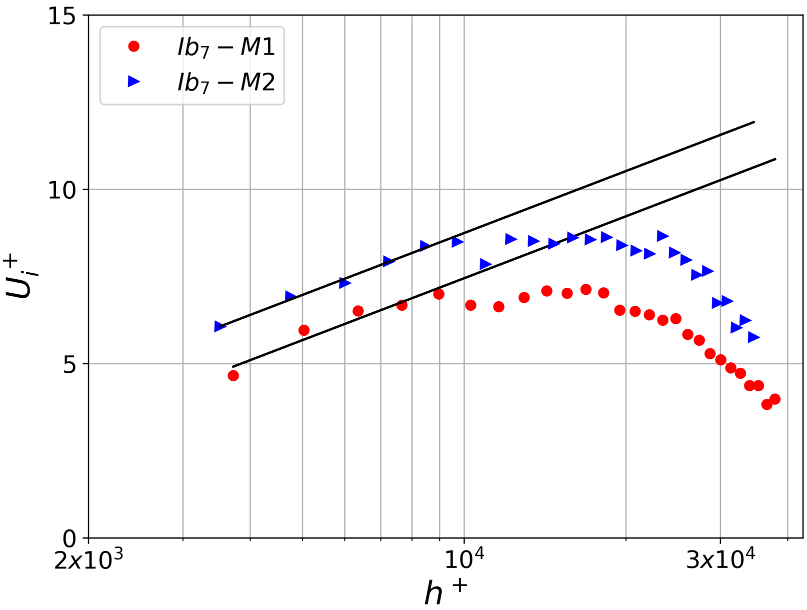

Figure 15. The sensitivity of the obtained values of $u_b^\star$ and z_0 from the logarithmic fitting (section 2.4) to a short period of measurement. Two measurements ($M1$ and $M2$) with $T_\infty = 2$ minutes at Ib_7 are shown separately in wall units. While the value of $u_b^\star$ is consistent for both $M1$ and $M2$ (see Table 4), the values of z_0 is significantly different between $M1$ and $M2$.